metals

MDPI

Article

Effect of High-Energy Ball Milling Time on the Density and Mechanical Properties of W-7%Ni-3%Fe Alloy

Aleksey V. Nokhrin *, Nataliya V. Malekhonova *, Vladimir N. Chuvil'deev, Nikolay V. Melekhin, Anatoliy M. Bragov, Andrey R. Filippov, Maksim S. Boldin, Eugeniy A. Lantsev and Nikita V. Sakharov

Materials Science Department, Physical and Technical Research Institute, Lobachevsky State University of Nizhny Novgorod, 603022 Nizhny Novgorod, Russia; chuvildeev@nifti.unn.ru (V.N.C.); melehin@nifti.unn.ru (N.V.M.); bragov@mech.unn.ru (A.M.B.); filippov@mech.unn.ru (A.R.F.); boldin@nifti.unn.ru (M.S.B.); elancev@nifti.unn.ru (E.A.L.); nvsaharov@nifti.unn.ru (N.V.S.)

* Correspondence: nokhrin@nifti.unn.ru (A.V.N.); malekhonova@nifti.unn.ru (N.V.M.)

Abstract: The present work was aimed at the investigation of the effect of high-energy ball milling (HEBM) time on the sintering kinetics, structure, and properties of the heavy tungsten alloy (HTA) W-7%Ni-3%Fe. The HTA samples were obtained from nanopowders (20–80 nm) using conventional liquid-phase sintering (LPS) in hydrogen and using spark plasma sintering (SPS) in vacuum. The HTA density was shown to depend non-monotonously on the HEBM time that originates from the formation of nonequilibrium solid solutions in the W-Ni-Fe systems during HEBM. The SPS kinetics of the HTA nanopowders was shown to have a two-stage character, the intensity of which depends on the Coble diffusion creep rate and on the intensity of diffusion of the tungsten atoms in the crystal lattice of the γ-phase. The kinetics of sintering of the initial submicron powders has a single-stage character originating from the intensity of the grain boundary diffusion in the γ-phase. The dependencies of the hardness and of the yield strength on the grain sizes were found to obey the Hall–Petch relation. The hardness, strength, and dynamic strength in the compression tests of the fine-grained tungsten alloys obtained using SPS and LPS were studied.

Keywords: tungsten alloys; nanopowders; high-energy ball milling; spark plasma sintering; strength

check for updates

Citation: Nokhrin, A.V.; Malekhonova, N.V.; Chuvil'deev, V.N.; Melekhin, N.V.; Bragov, A.M.; Filippov, A.R.; Boldin, M.S.; Lantsev, E.A.; Sakharov, N.V. Effect of High-Energy Ball Milling Time on the Density and Mechanical Properties of W-7%Ni-3%Fe Alloy. *Metals* **2023**, *13*, 1432. https://doi.org/10.3390/met13081432

Academic Editor: Jiro Kitagawa

Received: 17 April 2023
Revised: 31 July 2023
Accepted: 4 August 2023
Published: 10 August 2023

Copyright: © 2023 by the authors. Licensee MDPI, Basel, Switzerland. This article is an open access article distributed under the terms and conditions of the Creative Commons Attribution (CC BY) license (https://creativecommons.org/licenses/by/4.0/).

1. Introduction

Heavy tungsten alloys (HTAs) of the W-Ni-Fe system with W content over 85–90% have a number of unique characteristics: simultaneous increased density, strength, and plasticity at room temperature [1–5], high characteristics of dynamic strength [6,7], high radiation resistance, etc. Industrial tungsten alloys with 90–95% W obtained using conventional liquid-phase sintering (LPS) have a density of 17–19 g/cm^3, an ultimate strength of up to 1000 MPa, and elongation to failure of up to 25–30% at room temperature [8]. Additional strain strengthening allows for improving the ultimate strength to up to 1400–1600 MPa, preserving satisfactory ductility [8–12]. These features make HTAs interesting for various construction applications as well as interesting objects for investigations of the effect of the interphase boundaries on the mechanical properties of the alloys [13–16].

It Is worth noting that the technologies of strain hardening of HTAs have approached the limits of their capabilities at present. For further improving the properties of HTA, modern technologies of powder metallurgy are often used [17,18] including additive manufacturing methods [19–21] and the microwave sintering method [22]. Modern methods of the fabrication of the nanopowder composition W-Ni-Fe are being developed extensively [5,19,23].

Analysis of the literature shows spark plasma sintering (SPS) to be one of the promising methods of fabricating HTAs [24–28]. An opportunity to vary the main process parameters affecting the microstructure parameters of HTAs, most essentially (the heating rate, the temperature and time of sintering, the magnitude of the pressure applied, etc.) directly

in the course of sintering, provides great flexibility to the SPS method in controlling the mechanical properties of the HTAs. The opportunity of sintering the materials at very high heating rates (up to 2500 °C/min) is an important feature of SPS technology, which allows for reducing the grain growth rate [24,28]. The fine-grained HTAs obtained using SPS simultaneously have high strength and hardness [29–45] (Table A1; see Appendix A).

High-energy ball milling (HEBM) is one of the most efficient ways to produce tungsten-based nanopowders [46–49]. Compared with other production methods such as freeze-drying, [50], wet chemical processes [51], hydrogen annealing of tungsten oxides [52], spray drying [53], and DC arc plasma chemical synthesis [19,23], HEBM is the most efficient and productive process due to the simplicity of its equipment and process procedure. Currently, mechanical milling is widely used as the main method to produce tungsten-based nanopowders [54]. Thus, Malewar et al. [55] demonstrated the effectiveness of HEBM by obtaining high-density HTA samples via sintering at 1790 °C. However, despite the apparent simplicity of the process, the final powder particle size and quality depend on a number of variables. The essential parameters for HEBM are milling time, milling speed, feed ratio, temperature, milling atmosphere, milling media, etc. Depending on the grinding time, the final particle size may vary, and the material of the container and balls may affect the degree of contamination of the resulting powder [56]. An important disadvantage of HEBM technology that needs to be taken into account is the increased agglomerability of tungsten nanopowders. Currently, there are not many data in the literature that explain the nature of the influence of certain mixing parameters on the properties of the powder and the final product. Thus, Kiran et al. [57] showed that milling media play a crucial role in determining the purity of the final powder, and that increasing the milling time can significantly reduce the size of tungsten particles. It was also shown by the authors that increasing the HEBM time increases the density of the final product. In [58], it was shown that introducing additional defects in tungsten particles in the HEBM process makes it possible to reduce the onset temperature for the sintering of powder blanks, as well as to make the microstructure more homogeneous. A nonmonotonic dependence of hardness and fracture resistance on milling time was also observed [58]. Malkin's group showed that HEBM changes the adsorption properties of tungsten powders [59], changes the heat capacity of tungsten powders [60], and leads to the formation of strong internal stresses and microstrains of the crystal lattice of tungsten powders and increases their reactivity [61]. Thus, HEBM is an effective method for changing the size, structure, and properties of tungsten powders.

Joint application of high-energy ball milling and SPS is one of the promising methods of further improving the mechanical properties of HTAs [1,2,9,10,13–18]. This allows for ensuring outstanding increases in the strength and hardness of the HTAs (Table A1; see Appendix A). It is interesting to note that the results of [28,29,34,40] evidence the possibility of the formation of a strongly supersaturated solid solution of tungsten in the γ-phase based on nickel during HEBM that leads to an additional acceleration of sintering of W-based nanopowders. The formation of the supersaturated solid solution of tungsten atoms in the γ-phase leads to the manifestation of some unexpected effects. The effect of the nonmonotonous dependence of the density on the sintering temperature [29,30,36,44,45,62], as well as the effect of the reduction in the activation energy of sintering of the nanopowders [62], deserve a high amount of attention. One should note separately the effect of decreasing the density of tungsten alloys sintered from mechanically activated nanopowders [34,40,62], the nature of which remains unclear now. Also, the effect of nonmonotonous (with a maximum) dependencies of the HTA density on the time of preliminary HEBM of the powders observed in [62] is interesting.

From a practical viewpoint, the results of increases in the hardness, the static strength, and the dynamic strength of the HTAs obtained using SPS are important.

Analysis of the literature shows that the W-7%Ni-3%Fe alloys obtained via SPS from nanopowders (t_{HEBM} = 20 min) have a higher dynamic strength as compared with coarse-grained alloys [43,63]. The decrease in the grain sizes was noted to result in simultaneous

increases in the static strength, the dynamic strength, and in the penetration depth of an HTA sample into a steel barrier. At a throwing speed of 1194 m/s, the penetration depth reached 15.2 mm, whereas for coarse-grained HTAs this magnitude varied from 9.4 to 12.8 mm under similar testing regimes [63]. The formation of a strongly supersaturated solid solution in the γ-phase may be one of the origins of the manifestation of increased dynamic strength of the HTAs. In our opinion, this allows for increasing the strength of the interphase (α-γ) boundaries and, as a consequence, ensuring additional increases in the strength of HTAs.

The investigation of the effect of the HEBM time (t_{HEBM}) of the powders on the density, microstructure parameters, and mechanical properties of the heavy tungsten alloy W-7%Ni-3%Fe obtained via SPS was the main goal of the present work.

2. Materials and Methods

The object of investigation was W-7%Ni-3%Fe alloy. The chemical compositions of the initial powders α-W, β-Ni, and α-Fe are presented in Table 1. The mean particle sizes in the initial powders α-W, β-Ni, and α-Fe according to Fischer were R_0 = 0.8 μm, 20 μm, and 11 μm, respectively.

Table 1. Chemical compositions of initial powders (wt.%).

Powders	O	Fe	C	S	P	Ni	Co	Si	Cu	Mo	Mn
α-W	8×10^{-2}	2×10^{-2}	1×10^{-2}	-	5×10^{-3}	1×10^{-2}	-	5×10^{-3}	1×10^{-2}	4.5×10^{-2}	2×10^{-3}
β-Ni	3×10^{-1}	1.5×10^{-3}	1×10^{-1}	6×10^{-4}	1×10^{-3}	balance	7×10^{-4}	1×10^{-3}	1×10^{-3}	-	3×10^{-4}
α-Fe	2×10^{-1}	balance	4.8×10^{-2}	4×10^{-3}	-	-	-	1×10^{-2}	-	-	-

The initial coarse-grained compositions were obtained by mixing the powders α-W, β-Ni, and α-Fe in a FRITSCH® Pulverisette 6 planetary ball mill (Idar-Oberstein, Germany). The mixing time was 15 h and the mixing rate was 100 rpm. A preliminary stage of long stirring allows for a homogeneous distribution of β-Ni and α-Fe powders in submicron α-W powders. HEBM of the composition W-7%Ni-3%Fe was performed in APF-3 high-energy planetary mill (Russia). The acceleration of the milling bodies was 60 g and the mixing rate was 1450 rpm. The containers and milling balls of 6–10 mm in diameter were made from industrial alloy W-7%Ni-3%Fe. The mass ratio of the balls and the powders was 10:1. HEBM with durations of 5, 10, 20, and 40 min was performed in argon ambient gas with addition of ethanol. To minimize the heating of the powders, HEBM was performed in several stages, each 5 min long. During HEBM, large and small agglomerates consisting of nanoparticles were formed. The presence of large agglomerates in the powder hinders the sintering process and can lead to the formation of large pores. Large agglomerates of several hundred microns in size were eliminated using a set of sieves with different mesh sizes. The minimum mesh size was 50 μm.

The HTA samples were obtained by conventional sintering in hydrogen (Method I) and by SPS (Method II).

To obtain the HTA samples using Method I, the nanopowders were pressed into samples of 30 mm in diameter and 5–6 mm in height in advance. Uniaxial pressing with a pressure of 150 MPa was performed at room temperature in a steel mold. The powders had a bulk density of ~7 g/cm^3 after 20–40 min of HEBM. The density of the green body was ~9 g/cm^3. The density was measured by weighing the body and measuring its geometric dimensions. The error in determining the density of the green body was 0.1–0.2 g/m^3. The final dimensions of the samples depended on the sintering temperature and density of the sintered material.

The sintering was performed in a two-stage regime: Stage I—heating with the rate 25 °C/min up to 950 °C and holding for 2 h for the reduction of the powders and removing oxygen; Stage II—heating up to the sintering temperature (1250, 1300, 1350, or 1400 °C) in 100 min and holding for t_s = 1 h. Sintering of samples was carried out in a hydrogen resistance furnace with a nominal power of 3 kW (380 V, 50 Hz). Heating and holding

of samples were carried out in hydrogen. Hydrogen consumption during sintering was 0.2–0.6 m^3/h. The sintered pressings were placed on a molybdenum table, on the surface of which aluminum oxide powder was poured to prevent the pressings from sticking to the table. The temperature was measured with tungsten–rhenium thermocouples. The accuracy of measuring the temperature was ±6 °C. After sintering, the samples were subjected to annealing in vacuum (10^{-5} Torr) at 1000 °C, 2 h. As the reference samples, the coarse-grained alloys W-7%Ni-3%Fe obtained by sintering the coarse-grained powder compositions in hydrogen were used.

Method II was implemented using Dr. Sinter model SPS-625 setup (SPS SYNTEX Inc., Japan). The sintering of samples of 30 mm in diameter and 4–4.5 mm in height was performed in vacuum (6 Pa) when applying a uniaxial pressure of 70 MPa. A single-stage sintering regime was used: heating with a rate of 100 °C/min up to the sintering temperature (1200 °C). The uniaxial pressure was applied simultaneously with the beginning of heating. Holding at the sintering temperature was not performed (t_s = 0 min). The temperature was measured with an optical pyrometer, Chino IR-AHS2 (Chino Corporation, Tokyo, Japan), focused onto the surface of the graphite mold. The uncertainty of the temperature measurement was ±5 °C. As the reference samples, nanopowders after HEBM that were subjected to annealing in hydrogen at 900 °C, 1 h in advance (before SPS) were used.

In the course of heating up, the effective shrinkage (L_{eff}, mm) and shrinkage rate (S_{eff}, mm/s) of the nanopowders were measured using a dilatometer. The contribution of the thermal expansion (L_0, mm) of the graphite mold and punch was taken into account on the basis of the results of experiments with empty mold. The temperature curves of shrinkage of the nanopowders (L, mm) were calculated according to the following formula: $L(T) = L_{eff}(T) - L_0(T)$.

The residual graphite was removed from the surfaces of the sintered samples of 30 mm in diameter via waterjet cleaning. Mechanical grinding was performed using Struers Secotom 10 setup (Struers, Copenhagen, Denmark), and polishing was performed using Buehler Automet 250 setup (Buehler, Braunschweig, Germany). In the course of mechanical treatment, layers of ~300–350 μm, in which an increased carbon concentration can be observed due to high-temperature interaction of the material with the graphite mold, were removed from the sample surfaces [64,65].

The microstructure investigations of the alloys were carried out using Leica IM DRM optical metallographic microscope (Leica Microsystems GmbH, Wetzlar, Germany), Jeol JSM-6490 scanning electron microscope (SEM, Jeol Ltd., Tokyo, Japan), and TESCAN Vega 2 SEM (Tescan Orsay Holding, a.s., Brno, Czech Republic) with Oxford Instruments INCA 350 EDS microanalyzer (Oxford Instruments pls., Oxford, England). The average tungsten grain size (d) was determined with the chord method using GoodGrains 2.0 software (Russia). The density of the samples was measured via hydrostatic weighting in distilled water using Sartorius CPA balance (Sartorius AG, Göttingen, Germany). The uncertainty of the density measurement was ±0.01 g/cm^3. The magnitude of the theoretical density was accepted to be equal to ρ_{th} = 17.245 g/cm^3. The analysis of the chemical compositions was performed using Ultima 2 ICP atomic-emission spectrometer (HORIBA Jobin Yvon Inc., Edison, USA) and Leco RHEN-602 analyzer (LECO Corp., St. Joseph, MI, USA). X-ray diffraction (XRD) phase analysis was performed using Shimadzu XRD-700 diffractometer (Shimadzu, Kyoto, Japan) (CuK_α emission, λ = 1.54056 Å, scan rate 0.5 °/min, exposure 2 s, step 0.02°). The phase analysis of the samples was performed using Rietveld method. The contribution of the apparatus broadening into the XRD peaks was taken into account according to [62]. The analysis of internal stresses and calculation of the sizes of coherent scattering regions (CSR) were performed using Williamson–Hall method [66].

To study the mechanical properties of the sintered samples, the stress–relaxation testing technique was used, allowing for determining the magnitudes of the macroelasticity stress (lattice friction stress) (σ_0) and of the yield strength (σ_y) in the compression tests [62]. To measure σ_0 and σ_y, cylindrical samples of 3 mm in diameter and 6 mm in height were used. The uncertainties in measuring σ_0 and σ_y were ±20 MPa. The microhardness (Hv)

of the alloys was measured using HVS-1000 hardness tester (INNOVATEST Europe BV, Maastricht, The Netherlands) at a load of 1 kg.

The magnitude of compressive dynamic ultimate strength (Ys) was investigated with Kolsky bar method using Hopkinson split rod at the strain rate of ~10^3 s^{-1} [67]. An example of a dynamic strain curve of a tungsten alloy is presented in Figure 1. The ballistic characteristics of the material were determined by measuring the penetration depth (H) of a sample 3 mm in diameter and 25 mm long (Figure 2a) into a steel target of 30 mm in thickness. The samples were accelerated with a 12 mm two-stage gas gun powered by compressed air. The steel hardness was 27–30 HRC. The impact angle of the sample with the steel plate was 90°. The test procedure was described in [63]. The samples for testing were cut out from the central parts of workpieces of 30 mm in diameter by spark cutting in distilled water. The penetration depth of the sample was measured on a metallographic cross-section with Leica IM DRM optical microscope using GoodGrains 2.0 software (Figure 2b). Figure 2b shows a fragment of the cross-section of the target—a steel plate, in which a non-through hole was formed after the test. For convenience of the microstructure investigations, the steel samples were pressed into WEM REM mixture (Cloeren Technology GmbH, Berlin, Germany), the polymerization temperature of which did not exceed 150 °C; the polymerization time was 10 min. The uncertainty of determining the magnitude of H was ±0.1 mm. The increased error in determining the penetration depth H is due to the plastic deformation of the steel target in the impact zone. This resulted in curvature of the flat surface of the steel target and formation of irregularities near the impact area (Figure 2b).

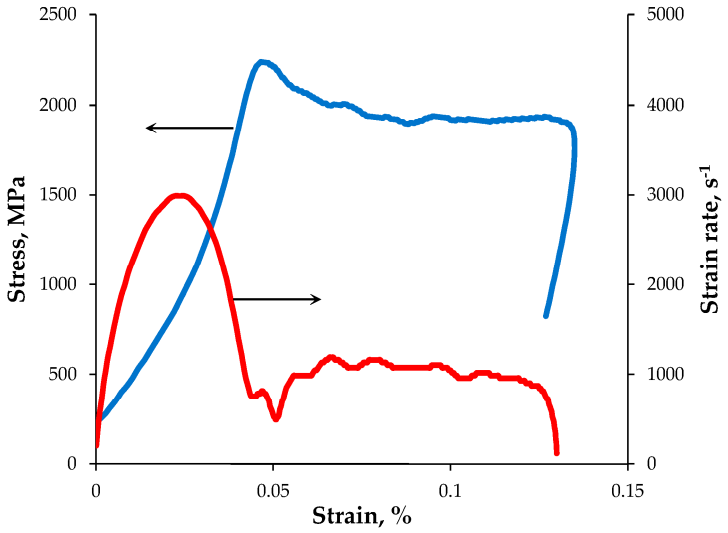
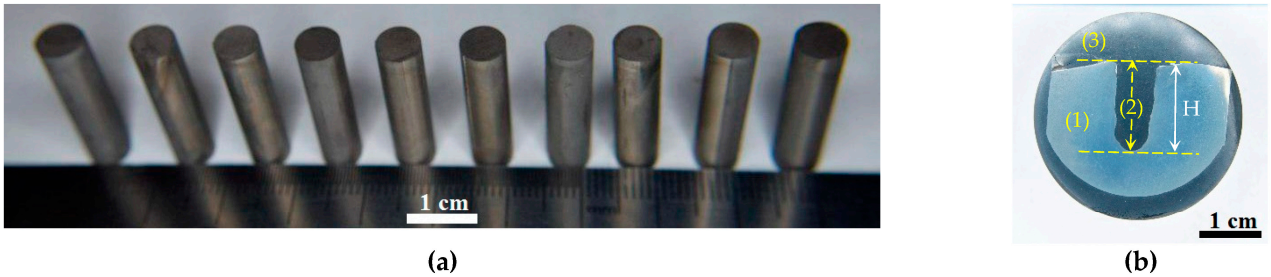


Figure 1. Typical stress–strain and strain rate–strain curves for a tungsten alloy sample recorded in a dynamic compression test according to Kolsky bar method.



(a) **(b)**

Figure 2. Tungsten alloy samples for testing (**a**) and example of measuring the sample penetration depth into the steel target (**b**). (**b**): (1) steel target, (2) hole in target from tungsten sample, (3) WEM REM mixture.

3. Results

3.1. Investigation of the Powders

Figure 3 presents the images of the powders of the W-7%Ni-3%Fe compositions in their initial state, after mixing in the FRITSCH® Pulverisette 6 planetary ball mill (32 h, Figure 3a) and after HEBM for different processing times (Figure 3b–f). Figure 3e shows an image of the surface of the fractured fine agglomerate. Individual submicron tungsten particles are visible on the surface. Figure 3f shows the surface image of an undestroyed fine agglomerate.

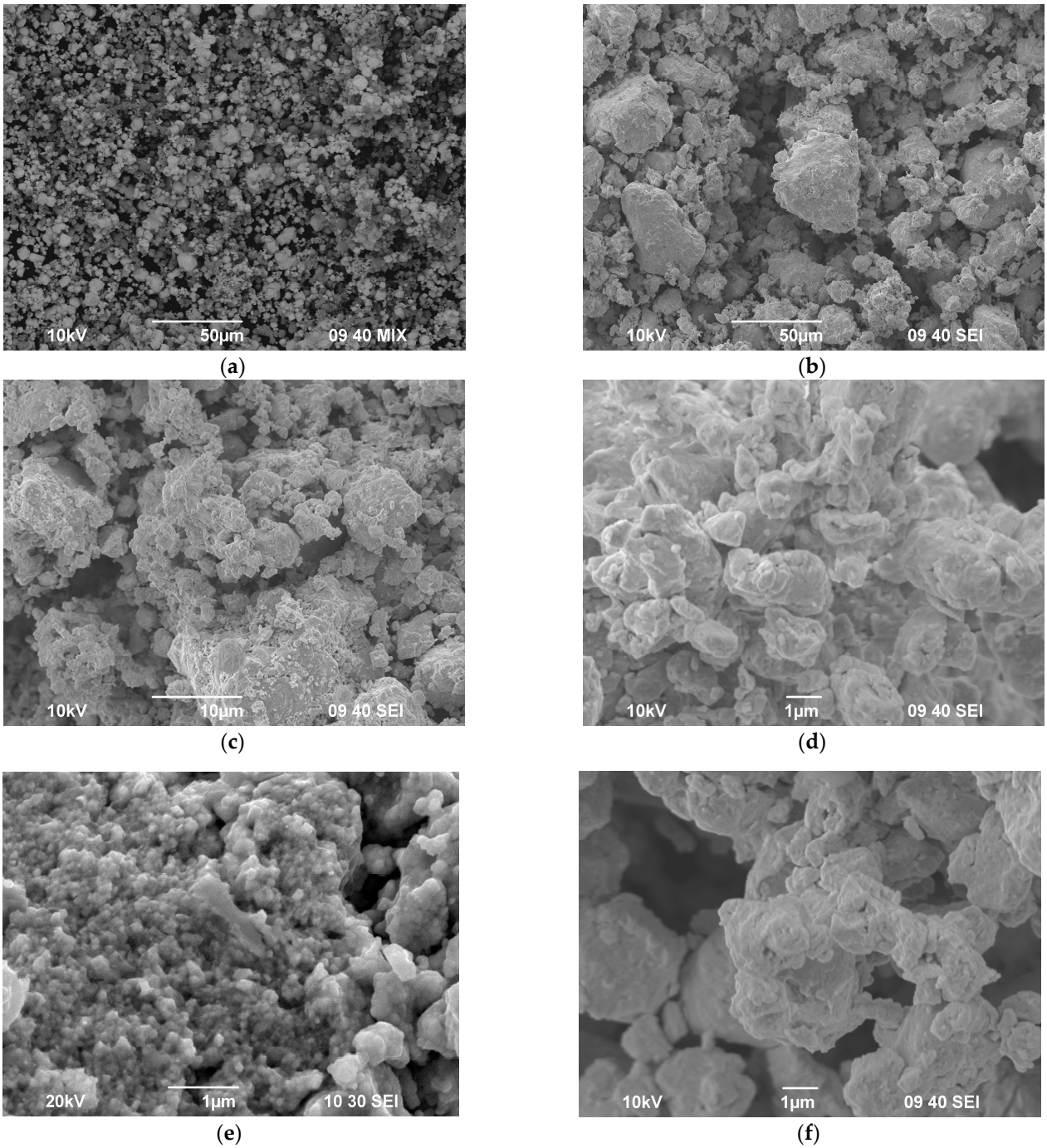
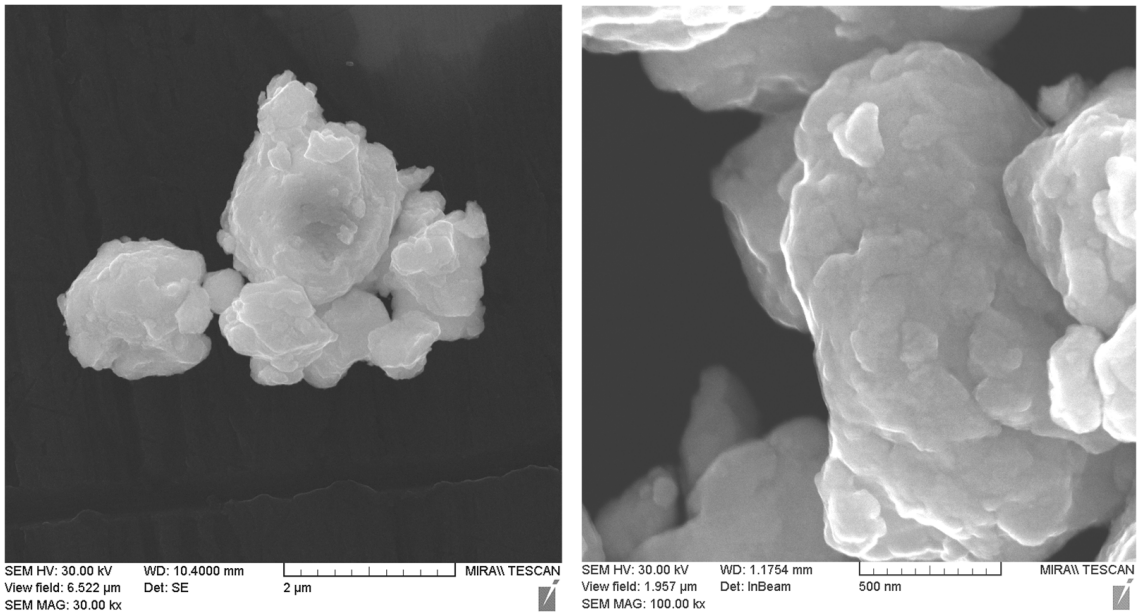


Figure 3. SEM images of W-7%Ni-3%Fe powder agglomerates for different HEBM times: (**a**) 0 min; (**b**) 5 min; (**c**) 10 min; (**d**) 20 min; (**e**,**f**) 40 min.

As one can see in the images presented in Figure 3, sufficiently large micron-sized agglomerates consisting of several tens of nanoparticles with splinter shapes (Figure 4a) or round shapes (Figure 4b) form in the course of HEBM. The complex morphology of the nanopowder after HEBM is related to the impact of grinding bodies on W-Ni-Fe particles. At a high rotational speed, the grinding bodies impact the powder particles, thereby breaking them into smaller particles, as well as carrying out their intensive plastic deformation. As the milling time increases, the number of impacts of the milling bodies on the particles increases, thereby increasing the degree of fragmentation of the powder particles and increasing the degree of their deformation. The presence of relatively ductile Ni and Fe particles leads to the agglomeration of stronger W particles.



(**a**) (**b**)

Figure 4. SEM images of the nanoparticles in the powder agglomerates 90%W-7%Ni-3%Fe for different HEBM times: (**a**) t_{HEBM} = 10 min; (**b**) t_{HEBM} = 40 min.

The results of the XRD phase analysis show that a decrease in the intensity and the broadening of the XRD peaks of α-W take place in the course of HEBM (Figure 5a). No peaks corresponding to iron and nickel were visible in the XRD curves. This suggests that a strong fragmentation of the Ni and Fe particles takes place during HEBM.

A shift in the tungsten peaks towards greater diffraction angles was observed (Figure 5b). The (110) α-W peak position in the initial coarse-grained powder corresponds to the diffraction angle $2\Theta_{max} = 40.26^\circ \pm 0.02^\circ$. After HEBM during t_{HEBM} = 40 min, the (110) α-W XRD peak shifted by ~0.08–0.12° up to $2\Theta_{max}$ = 40.34–40.38°. The (211) α-W peak position in the initial as-mixed powder corresponds to the diffraction angle $73.18^\circ \pm 0.02^\circ$. After HEBM during t_{HEBM} = 40 min, the (211) α-W XRD peak shifted up to 73.30–73.32°. The fact of the X-ray peak shift was additionally confirmed in experiments with increased exposure time (4 s). According to Wulff–Bragg's equation ($2d_{hkl} = n\lambda_{Cu} \cdot \sin 2\Theta_{hkl}$), this evidences that the compressive internal stress fields that form in the tungsten nanoparticles in the course of HEBM lead to a decrease in the interplanar distances d_{hkl}.

It is notable that one can see asymmetry in the tungsten XRD peaks in Figure 5b; the (110) α-W peaks are broadened more strongly towards the greater diffraction angle 2Θ. After HEBM for 40 min, the half width at half maximum (HWHM) of the (110) α-W peak at small diffraction angles was $\Theta_{-0.5}$~0.30–0.32°, whereas the one at large diffraction angles was $\Theta_{-0.5}$~0.42–0.44°. In the initial state, the (110) α-W peaks were highly symmetric ($\Theta_{-0.5} \sim \Theta_{+0.5}$~0.06–0.10°). According to [62], this result means that after HEBM, the nanoparticles have a core–shell structure; a strain-induced dissolving of nickel

and iron atoms in the surface layers of the α-W nanoparticles takes place during HEBM. This leads to the formation of internal compressive stress fields in the surface layers of the α-W nanoparticles and, as a consequence, to the broadening of the α-W peaks towards greater diffraction angles.

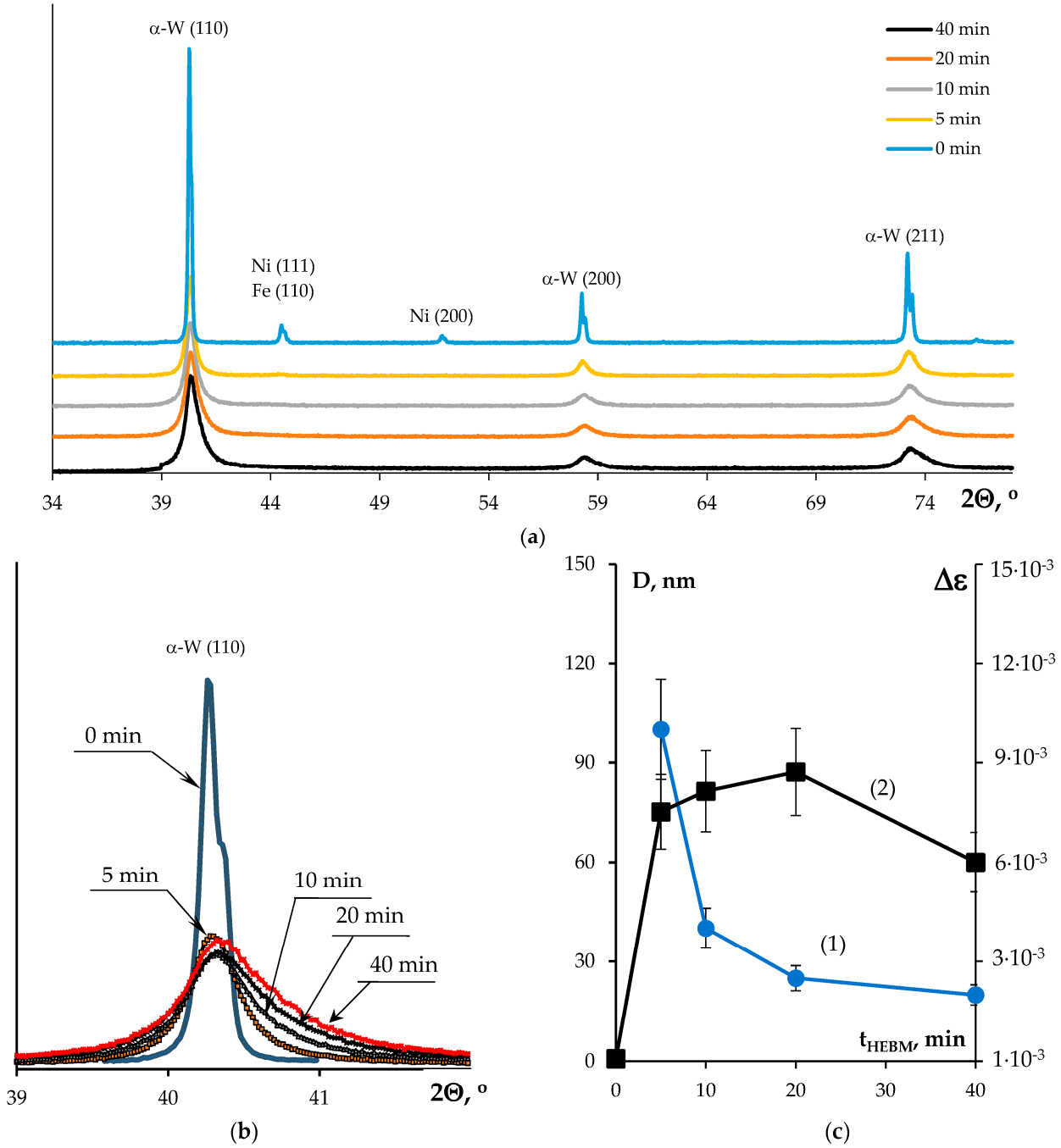


Figure 5. Results of XRD phase analysis of the powders 90%W-7%Ni-3%Fe: (**a**) overview XRD curves after different HEBM times; (**b**) effect of the HEBM time on the broadening of the (110) α-W peaks, data from [62]; (**c**) effect of the HEBM time on the CSR size (1) and on the magnitude of the microstrain Δε of the α-W crystal lattice (2), data from [62].

The calculations of the coherent scattering region sizes (D_{XRD}) according to the Williamson–Hall model show D_{XRD} to decrease from ~80–100 nm down to ~20–25 nm with an increase in t_{HEBM} from 5 up to 40 min. The estimates obtained evidence that the

agglomerates shown in Figure 3 consist of several tens or hundreds of tungsten particles on average.

It is worthwhile to pay attention to the nonmonotonous character of the dependence of the microstrain of the tungsten crystal lattice ($\Delta\varepsilon$), calculated according to the Williamson–Hall method, on the HEBM time. As one can see in Figure 5c, the maximum value $\Delta\varepsilon_{max}$~$9{\cdot}10^{-3}$ was achieved after 20 min of HEBM. At a further increase in the HEBM time, the magnitude of $\Delta\varepsilon$ decreased down to ~$6{\cdot}10^{-3}$. So far, one can conclude that essential compressive internal stress fields form in the tungsten nanoparticles in the course of HEBM, leading to a strong distortion of the α-W crystal lattice (see [52]).

The investigations of the chemical compositions show that the oxygen concentration in the nanopowders after HEBM reached 1.5–1.55 wt.%. These results agree qualitatively with the ones in [68], where an increase in the oxygen concentration in the tungsten powders after HEBM was also observed. During HEBM, the particle size decreases and the specific surface area of the powders increases. This leads to an increase in the concentration of oxygen adsorbed on the surface of the tungsten nanopowders. After being annealed in hydrogen at 900 °C (1 h), the oxygen concentration in the nanopowders decreased down to 0.8–0.95 wt.%. The parameters of the XRD peaks of α-W did not change after the nanopowders were annealed in hydrogen.

3.2. Sintering the Nanopowders in Hydrogen

The investigations of the macrostructure of the samples show that the sintering of the nanopowders at 1450 to 1500 °C leads to the formation of large pores (Figure 6). This leads to a decrease in the density of the samples sintered from the mechanically activated nanopowders (Table 2). Sintering at lower temperatures (1250, 1300, and 1350 °C) did not result in the formation of macropores. No macropores were observed when sintering the coarse-grained powders.

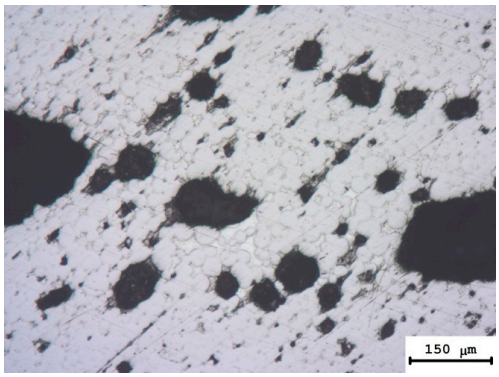


Figure 6. Appearance of the W-7%Ni-3%Fe alloy samples sintered in hydrogen from the nanopowders obtained using HEBM. Sintering temperature: 1450 °C. Metallography.

Table 2. Microstructure characteristics and mechanical properties of the W-7%Ni-3%Fe alloy samples obtained from the nanopowders by sintering in hydrogen.

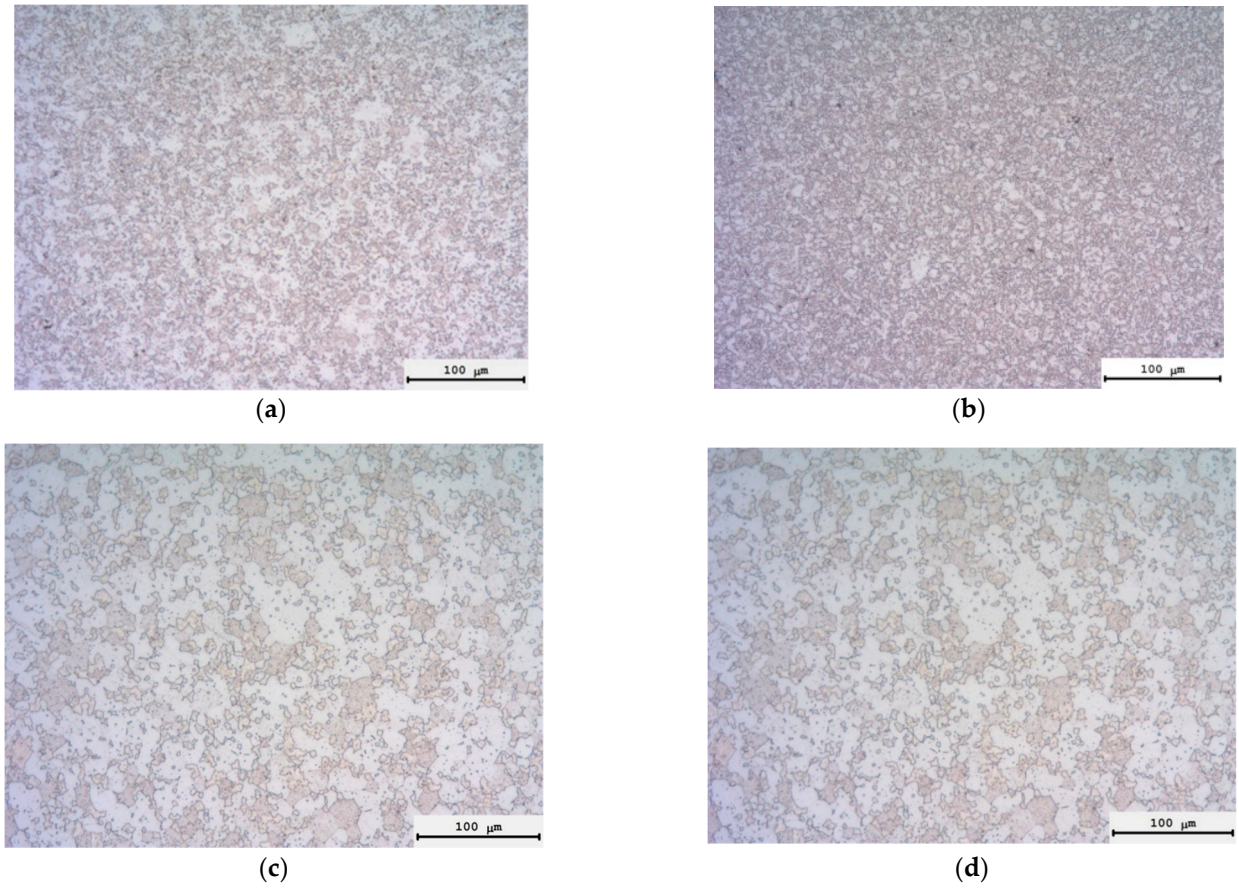
	Characteristics of Alloy Obtained from Coarse-Grained Powders							Characteristics of Alloy Obtained from Nanopowders						
T_s, °C	ρ, g/cm^3	d, μm	σ_0, MPa	σ_y, Mpa	Hv, Gpa	Ys, Mpa	H, mm	ρ, g/cm^3	d, μm	σ_0, Mpa	σ_y, Mpa	Hv, Gpa	Ys, Mpa	H, mm
1250	17.94	5–10	520	1150	4.2	1830	3.8	17.79	1–3	960	1540	7.9	1900	5.1
1300	18.02	~5–10	460	990	4.2	1700	4.2	17.93	1–3	1000	1340	7.5	2050	4.7
1350	18.06	~10	290	790	4.1	1650	4.2	17.95	1–3	860	1200	7.2	1870	3.7
1400	18.14	~20	230	740	4.0	1640	4.1	17.49	3–5	300	740	6.9	1500	3.1
1450	18.11	40–45	220	600	3.8	1590	3.7	17.05 [1]	~10	-	-	6.5	-	-
1500	18.06	~50	200	690	3.6	1580	3.2	16.87 [1]	~22	-	-	6.2	-	-

[1] The density was measured by measuring the mass and geometrical sizes of the samples.

The chemical reaction of hydrogen with oxygen adsorbed on the nanopowder particle surfaces is the most probable origin of the macropore formation. This reaction goes with the formation of water vapor: $2H_2 + O_2 = 2H_2O$ (see [69]). The removal of the water vapor from the nanopowders that were pressed in advance is difficult, leading to an increase in the gas pressure inside the micropores and, as a consequence, to the formation of large macropores at elevated temperatures. The second factor promoting macropore formation could be more intensive diffusion of hydrogen in the nanostructured HTAs. The investigations of the chemical compositions show that the hydrogen concentration in the samples sintered from the nanopowders reached 83–97 ppm (T_s = 1450–1500 °C), while in the samples sintered from the coarse-grained powders, the hydrogen concentration varied from 2.6 to 11 ppm.

We assume that there are several reasons for the formation of large pores at temperatures of 1450–1500 °C. Preliminarily, it should be noted that the formation of large pores occurs at temperatures close to the melting temperature of the γ-phase. Under these conditions, acceleration of diffusion and grain growth processes is observed. Firstly, this can lead to accelerated accumulation of water vapor molecules in triple junctions of grain boundaries, as well as to accelerated diffusion of hydrogen from the furnace working chamber into the surface of the sintered sample. Secondly, intensive migration of grain boundaries leads to an increase in the characteristic scale of diffusion mass transfer. This leads to an increase in the time required for pore elimination by the diffusion mechanism. Thirdly, in the presence of internal gas pressure, the fusion of several small pores can lead to the formation of a larger pore (see [70]).

Table 2 presents the results of investigations of the density and mean grain sizes for the W-7%Ni-3%Fe alloy samples sintered in hydrogen at different temperatures. Figure 7 presents the microstructures of the HTA samples sintered in hydrogen from the nanopowders.



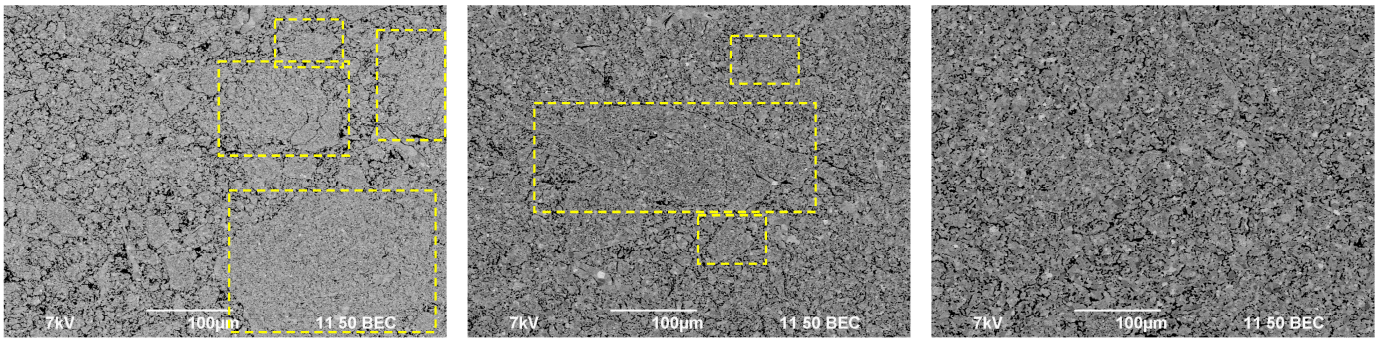
(**a**) (**b**)

(**c**) (**d**)

Figure 7. Microstructure of W-7%Ni-3%Fe alloy sintered from nanopowders (t_{HEBM} = 20 min). Sintering temperature T_s = 1250 °C (**a**,**b**), 1400 °C (**c**,**d**). Metallography.

Figure 7 shows that there are no large pores in the samples sintered at lower temperatures (1250–1400 °C). As the sintering temperature increases, grain growth is observed, and the microstructures of the samples become inhomogeneous. Analysis of the metallography results shows that increasing the sintering temperature up to 1250 and 1400 °C results in smooth increases in the mean tungsten particle sizes by up to ~1 μm and ~3–5 μm, respectively. The mean grain sizes in the samples sintered from the nanopowders were smaller than the ones in the samples sintered from the coarse-grained powders, but the alloy microstructure was sufficiently nonuniform.

The macroscopic inhomogeneities in the specimen microstructure were observed at the initial stages of sintering at the sintering temperatures 1150–1200 °C (Figure 8a,b). The degree of the microstructure's inhomogeneity decreases with increasing sintering temperature (Figure 8c). The presence of such inhomogeneities may be caused by the presence of large agglomerates in the nanopowders after HEBM.



(**a**) (**b**) (**c**)

Figure 8. Microstructure of the W-7%Ni-3%Fe alloy sintered from the nanopowder (t_{HEBM} = 20 min) at the temperatures 1250 °C (**a**), 1300 °C (**b**), and 1400 °C (**c**). Large agglomerates are highlighted with a yellow dashed line in Figure 8 for clarity. SEM.

The XRD phase analysis results show that the increase in the sintering temperature results in an increase in the intensity of the α-W XRD peaks; the asymmetry and the broadening of the peaks essentially decrease.

The increase in the mean grain sizes with increasing HTA sintering temperature from 1250 °C up to 1400 °C led to worsening of the mechanical properties of the alloy; the hardness decreased from 7.9 down to 6.9 GPa, the macroelasticity stress decreased from 960 down to 300 MPa, and the yield strength decreased from 1370 down to 620 MPa. It is notable that the mechanical properties of the samples sintered from the nanopowders at T_s = 1250 and 1300 °C were considerably better than those of the samples sintered from the coarse-grained powders (Table 2). Further increasing the annealing temperature (to over 1350 °C) led to a considerable decrease in the differences in the mechanical characteristics of the samples sintered from the coarse-grained powders and nanopowders.

3.3. Spark Plasma Sintering

Figure 9 presents the temperature curves of the shrinkage (Figure 9a,b) and those of the shrinkage rate (Figure 9c,d) of the nanopowders. Table 3 presents the results of investigations of the microstructure, density, and mechanical properties of these powders.

The analysis of the curves L(T) presented in Figure 9a shows the intensive shrinkage of the nanopowders to begin at lower temperatures as compared with the initial coarse-grained powders. The increase in the HEBM time from 5 up to 20 min leads to a shift in the temperature at the beginning of the intensive shrinkage stage from ~780–800 °C down to ~720 °C with a simultaneous increase in the maximum shrinkage L_{max} from ~2.6–2.7 mm up to 3.6–3.7 mm. The temperature at the end of the intensive shrinkage stage increases weakly with an increase in t_{HEBM} from 5 up to 20 min. Further increasing the HEBM time up to 40 min leads to an increase in the temperature at the beginning of the intensive

shrinkage stage up to ~750 °C and to a decrease in L_{max} down to ~3.0–3.1 mm. The similar character of the dependence $L_{max}(t_{HEBM})$ was observed for the annealed nanopowders (Figure 9b).

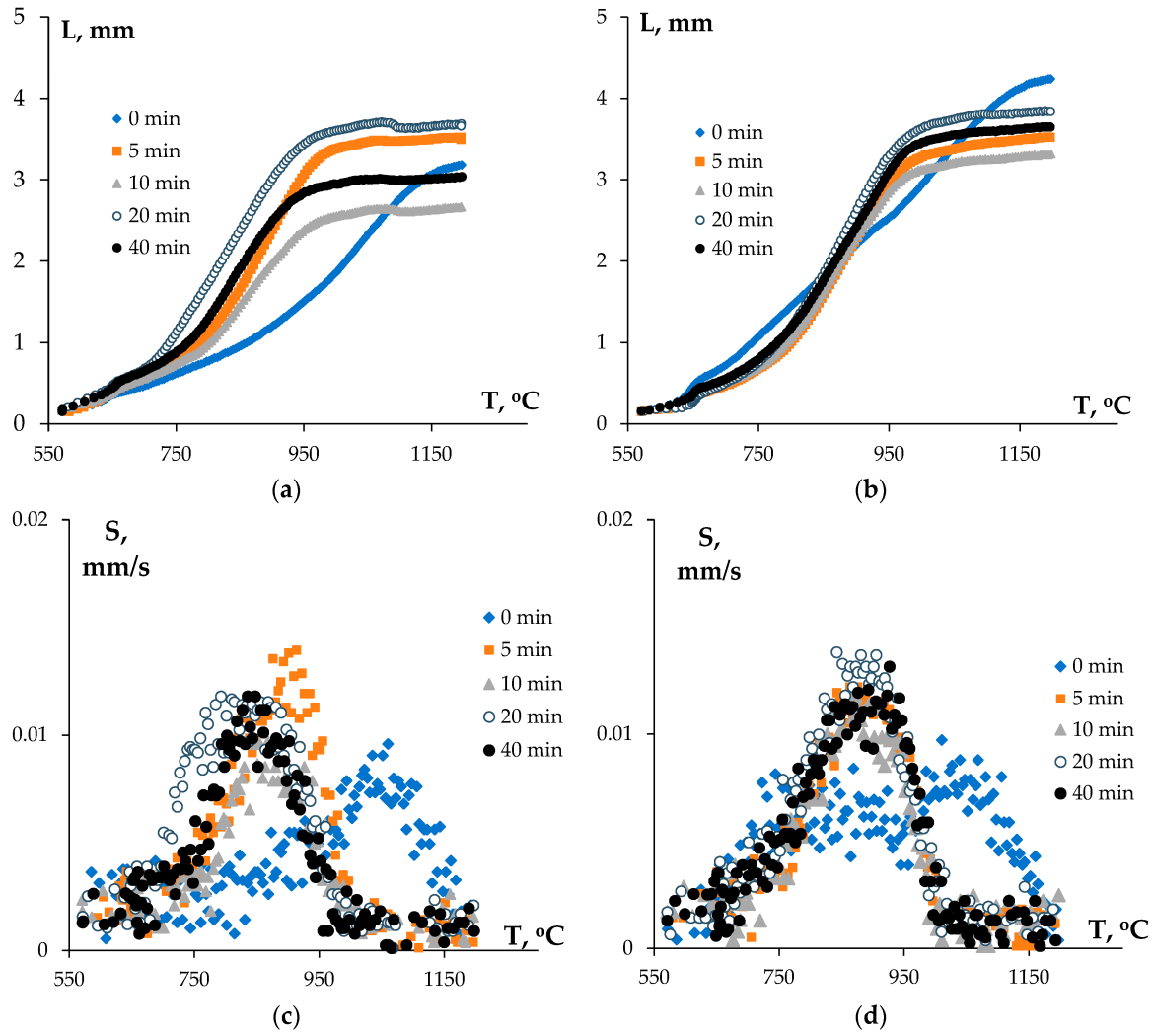


Figure 9. Temperature curves of shrinkage (**a**,**b**) and shrinkage rate (**c**,**d**) for the W-7%Ni-3%Fe nanopowders after HEBM (**a**,**c**) and after HEBM and annealing in hydrogen (**b**,**d**).

Table 3. Microstructure characteristics and mechanical properties of the W-7%Ni-3%Fe alloy samples obtained with SPS from nanopowders (T_s = 1200 °C).

	Characteristics of Alloy Obtained from Nonannealed Nanopowders							Characteristics of Alloy Obtained from Annealed Nanopowders					
t_{HEBM}, min	ρ, g/cm^3	d, μm	σ_0, MPa	σ_y, MPa	Hv, GPa	Ys, MPa	H, mm	ρ, g/cm^3	d, μm	σ_0, MPa	σ_y, MPa	Hv, GPa	Ys, MPa	H, mm
0	16.97	1.3	920	1850	4.2	-	4.9	17.02	1.2	1050	1930	4.3	-	5.1
5	16.64	0.9	1330	2160	4.5	2280	5.8	16.79	1.0	1400	2270	4.8	2350	5.1
10	16.45	0.8	1450	2180	4.7	-	5.7	16.92	0.7	1520	2310	4.9	-	5.4
20	15.68	0.7	1500	2370	4.8	-	5.7	16.31	0.6	1610	2350	5.3	-	6.6
40	16.78	0.7	1480	2350	4.7	2480	5.6	17.04	0.6	1530	2320	4.9	2630	6.1

As one can see in Figure 9b, the increase in the HEBM time leads to a shift in the curve S(T) towards lower temperatures and to an increase in the maximum shrinkage rate S_{max}. As one can see in Figure 9b, the maximum shrinkage rate for the coarse-grained

powders was observed at the temperatures ~1060–1080 °C; the shrinkage rate at those temperatures was S_{max} ~10^{-2} mm/s. Increasing the HEBM time up to 20–40 min leads to an increase in S_{max} of up to~(1.1–1.2) × 10^{-2} mm/s and to a decrease in the temperature corresponding to the maximum of the curve S(T) of up to 850–890 °C. In the case of the annealed nanopowders, the maximum shrinkage rate S_{max}~(1.3–1.4) × 10^{-2} mm/s was observed at the sintering of the nanopowders subjected to HEBM for 20 min.

Annealing in hydrogen affects the curves L(T) strongly and, to a lesser extent, the curves S(T). Comparing Figure 9a,b shows the annealing in hydrogen to result in an increase in the shrinkage of the initial coarse-grained powders. The scale for increasing the maximum shrinkage L_{max} for the annealed nanopowders was ~0.1–0.15 mm and depended weakly on the HEBM time. The annealing of the nanopowders in hydrogen leads to an insufficient decrease in the temperature corresponding to the maximum of the curve S(T) and to a weak increase in the maximum shrinkage rate S_{max}.

It is interesting to note that the densities of the samples depend on the HEBM time non-monotonously. As one can see from Table 3, the increase in t_{HEBM} from 0 up to 20 min leads to a decrease in the density from 16.97 down to 15.68 g/cm^3. After HEBM for 40 min, the densities of the samples increased by up to 16.78 g/cm^3. The dependence of density on the HEBM time for the samples sintered from the annealed nanopowders has a similar character. It should be stressed here that the annealing resulted in an increase in the densities of the sintered samples by ~0.1–0.2 g/cm^3.

The analysis of the results presented in Table 4 shows that increasing the HEBM time leads to a decrease in the mean grain sizes in the alloys sintered at 1200 °C. The mean grain sizes in the alloys sintered from the annealed and nonannealed powders were close to each other (Figure 10).

Table 4. SPS activation energies of W-7%Ni-3%Fe nanopowders.

t_{HEBM}, min	Nanopowders after HEBM				Nanopowders after HEBM and Annealing in Hydrogen			
	Stage II		Stage III		Stage II		Stage III	
	mQ_{s2}, kT_m	m	Q_{s2}, kT_m/kJ/mol	Q_{s3}, kT_m/kJ/mol	mQ_{s2}, kT_m	m	Q_{s2}, kT_m/kJ/mol	Q_{s3}, kT_m/kJ/mol
0	3.9	1/3	11.7/167	16.1/230	3.2	1/3	9.6/137	17.2/246
5	6.5		6.5/93	17.8/255	5.9		5.9/84	15.4/221
10	6.0	1	6.0/86	19.1/273	4.9	1	4.9/70	14.7/210
20	5.2		5.2/75	18.9/271	4.6		4.6/65	15.8/226
40	7.0		7.0/100	19.2/275	6.4		6.4/92	16.8/240

The HTAs obtained using SPS have a sufficiently uniform microstructure (Figures 10 and 11), in which few large grains are present. These grains are the recrystallized microstructure areas with minimal γ-phase content (Figure 11). Such large grains were observed in the samples obtained from the nanopowders with $t_{HEBM} \geq 10$ min most often. The volume fraction and sizes of the abnormally large grains in the samples sintered from the annealed nanopowders were considerably smaller than those in the samples sintered from the nonannealed nanopowders (Figure 10). This result suggests that the presence of the agglomerates after HEBM and increased oxygen concentration in the nanopowders are the most probable origins of the abnormally large grains that appear.

Figure 12 presents the results of XRD phase analysis of the samples obtained with SPS from the nanopowders. The analysis of the XRD curves presented shows the broadening of the α-W peaks in the sintered samples to be much lower than that in the nanopowders after HEBM. The asymmetry of the α-W XRD peaks in the sintered samples was absent, while the peak position $2\Theta_{max}$ was shifted towards smaller diffraction angles as compared with the one in the nanopowder. No essential differences in the characteristics of the (110) α-W peaks for the samples sintered from the nanopowders subjected to HEBM for different

times were observed (Figure 12b,c). This evidences that the intragranular stresses formed in the tungsten powders during HEBM relax in the course of sintering.

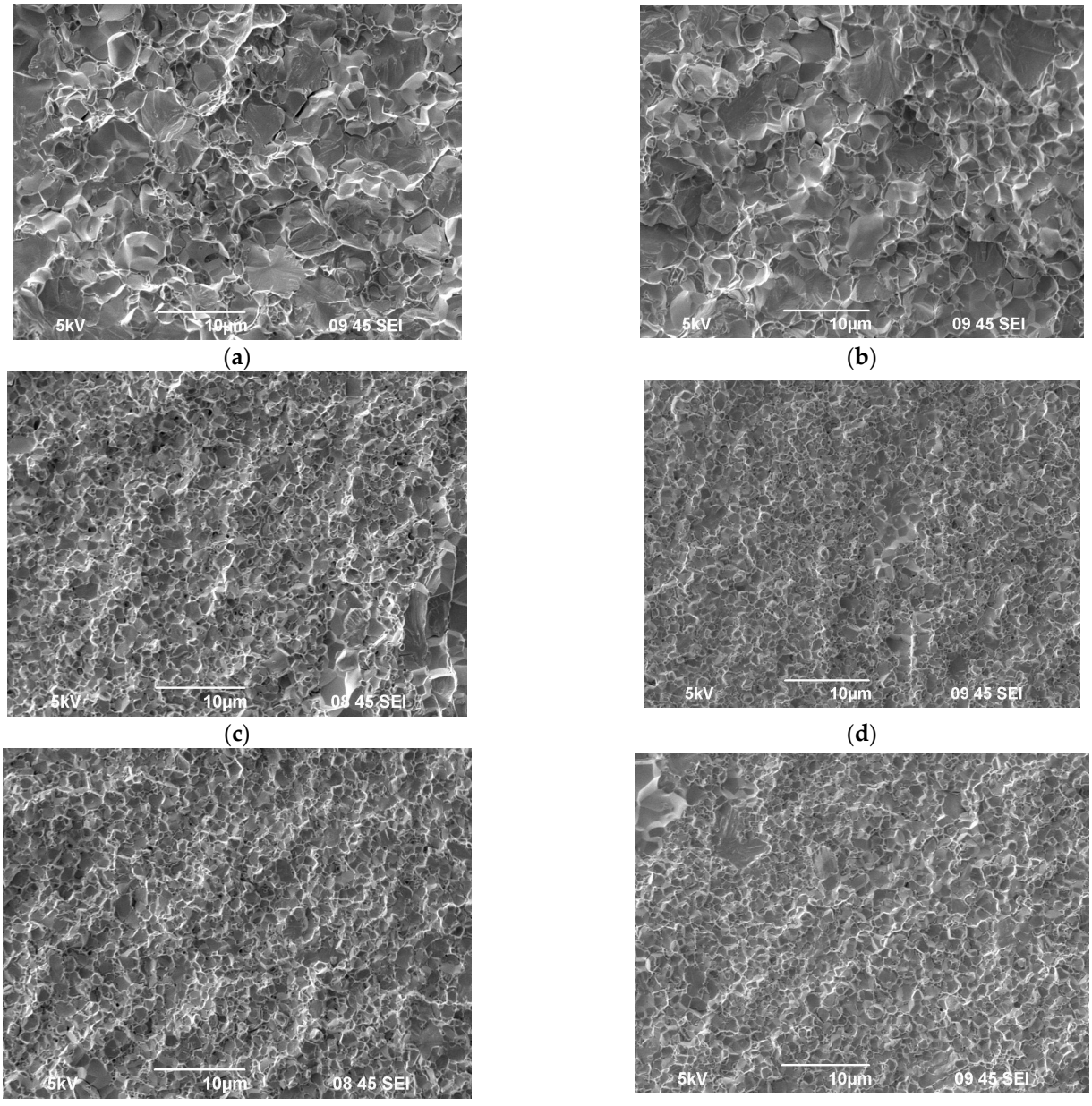


Figure 10. Microstructure of the W-7%Ni-3%Fe alloy obtained using SPS at 1200 °C from nonannealed (**a**,**c**,**e**) and annealed (**b**,**d**,**f**) nanopowders. HEBM time: (**a**,**b**) 0 min; (**c**,**d**) 10 min; (**e**,**f**) 40 min. SEM.

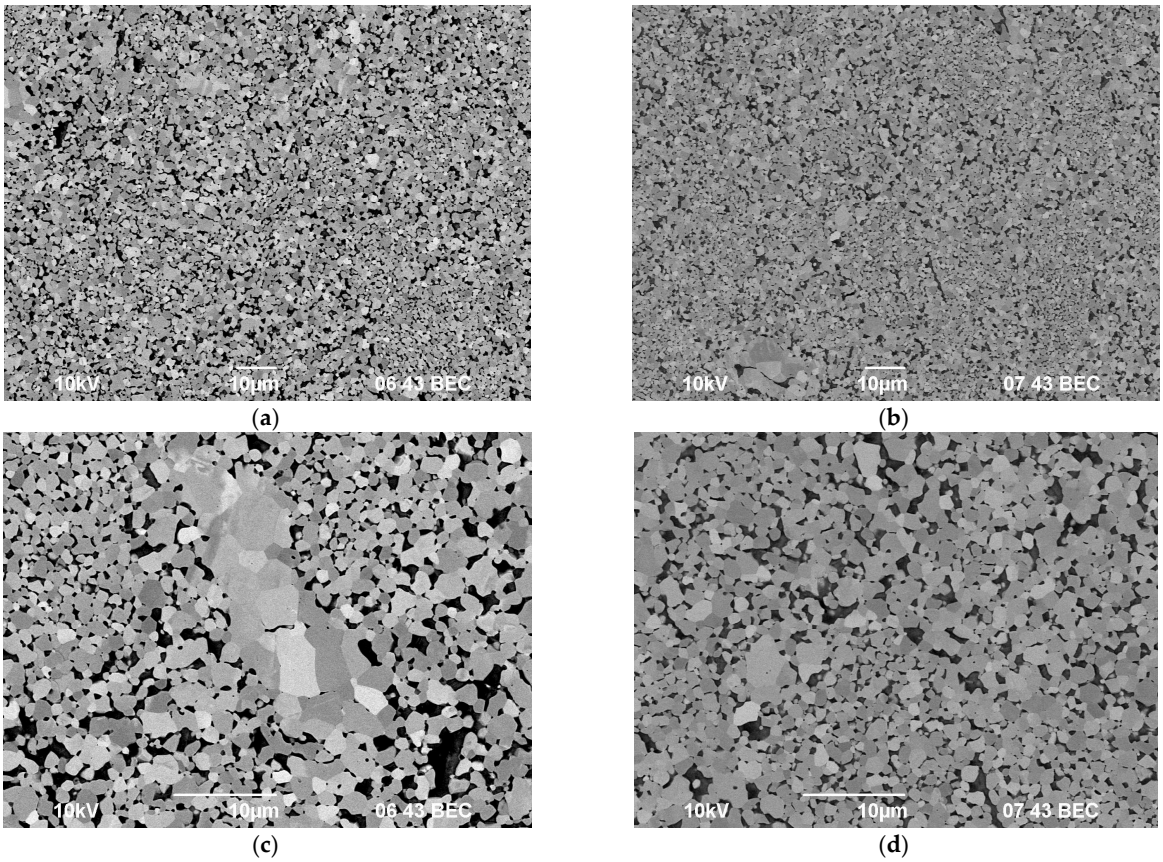
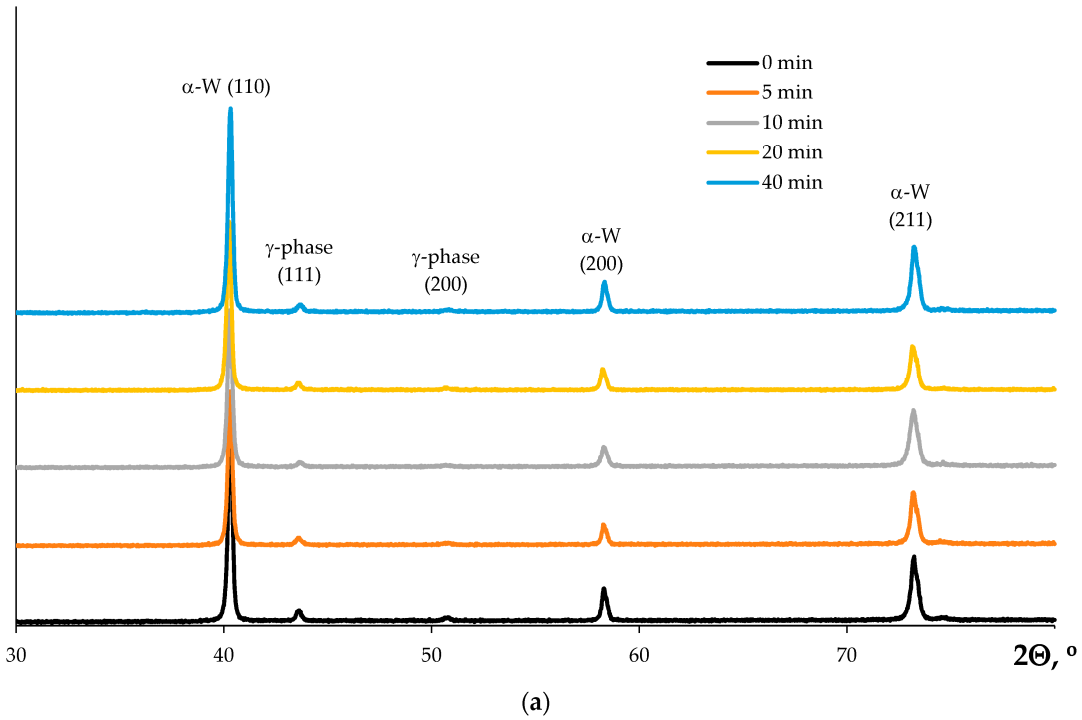


Figure 11. Microstructures of the samples obtained using SPS from the annealed (**a**) and nonannealed (**b**) nanopowders after HEBM (t_{HEBM} = 40 min). The areas with the abnormally large grains in the microstructure of the W-7%Ni-3%Fe alloy were obtained with SPS at 1200 °C from nonannealed (**c**) and annealed (**d**) nanopowders. t_{HEBM} = 40 min. SEM.



(**a**)

Figure 12. *Cont.*

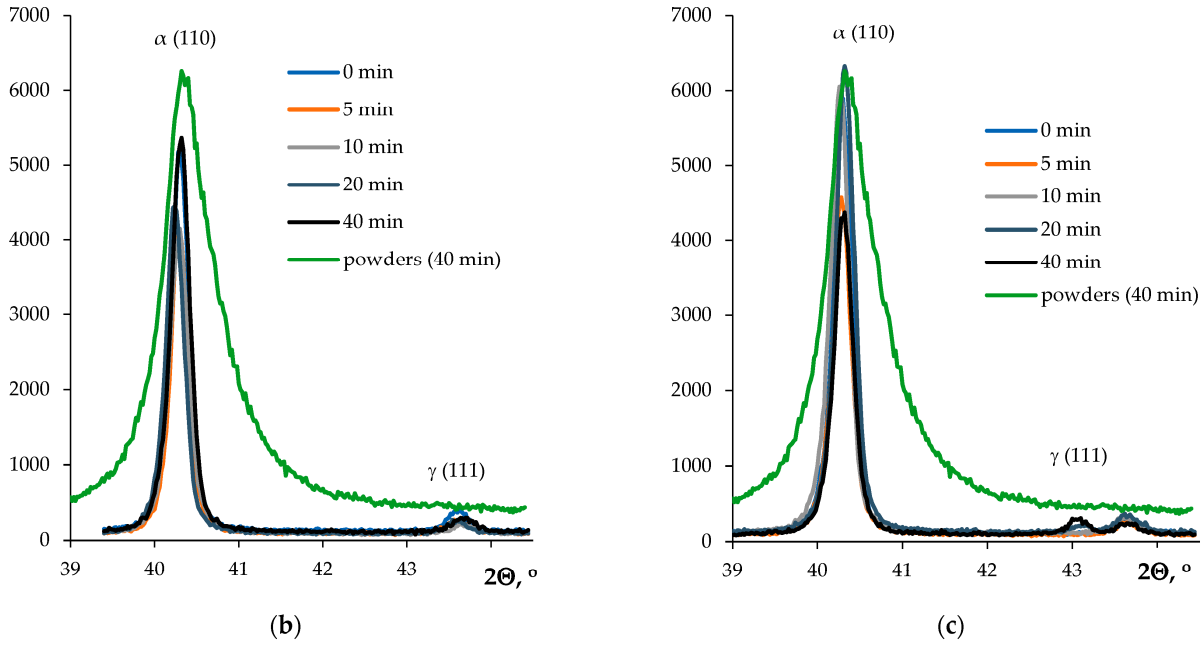


Figure 12. Results of XRD analysis of the W-7%Ni-3%Fe alloy obtained using SPS at 1200 °C (**a**). Effect of the HEBM time on the parameters of the (100) α-W peak in the samples sintered from the nonannealed (**b**) and annealed nanopowders (**c**).

The low-intensity γ-phase peaks are visible in the XRD curves of the sintered samples. Such peaks were absent in the XRD curves of the nanopowders after HEBM (Figure 5a,b). The characteristics of the XRD peaks from the γ-phase almost do not depend on the HEBM time (Figure 12b,c). No peaks of impurity phases were detected in the XRD curves (see [71]).

4. Discussion

The nonmonotonous dependence of the density of the samples obtained using SPS on the HEBM time (Figure 13) is one of the most interesting results obtained in the present work. Decreases in the alloy density from 98.4% down to 90.9% for the samples sintered from the nonannealed nanopowders and from 98.7% down to 94.6% for the ones sintered from the annealed nanopowders were observed when increasing HEBM time from 0 up to 20 min.

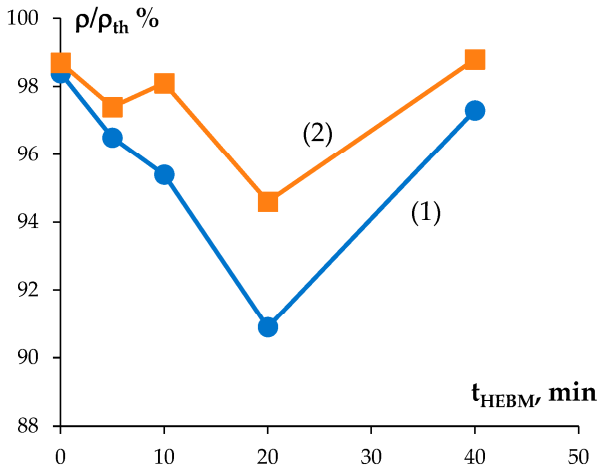


Figure 13. Dependencies of relative density of the W-7%Ni-3%Fe alloy sintered at 1200 °C on the HEBM time: (1) densities of the samples sintered from the nonannealed nanopowders; (2) densities of the samples sintered from the annealed nanopowders.

It is notable that large pores were absent in the microstructures of the sintered samples. The comparison of the microstructures of the samples sintered from the coarse-grained powders and from the nanopowders after t_{HEBM} = 20 min (Figures 8 and 9) did not reveal any essential increase in the sizes and volume fraction of the pores. So far, one can conclude that the decrease in the density of the alloy sintered from the nanopowders originates not from the increase in the volume fraction of the pores but from other factors. This conclusion is supported indirectly by the analysis of the curves L(T) and S(T) presented in Figure 7. As has been shown above, the maximum values of the shrinkage L_{max} and of the shrinkage rate S_{max} were observed in the case of SPS of the powders subjected to HEBM for 20 min.

To answer the question of the origin of the nonmonotonous dependence of the density on the HEBM time, we analyze the SPS mechanisms of the W-Ni-Fe nanopowders. First, it is worth noting that the characteristic sintering temperature T_s = 1200 °C is ~0.4 $T_{m(W)}$ and, according to [72], the diffusion intensity and the strain rate in tungsten are very low. (Here $T_{m(W)}$ = 3695 K is the melting point of tungsten [72]).

As one can see in Figure 9a,b, the curve L(T) has a usual three-stage character; the shrinkage of the nanopowders is finished almost completely within the intensive shrinkage stage (Stage II) in the temperature range from 750–800 °C to 1000–1050 °C. The intensity of shrinkage of the nanopowders within the third stage of sintering (T_s > 1000–1050 °C), at which the grain growth occurs, is often very low.

Analysis of the compaction kinetics of the nanopowders at Stage II can be made using the Young–Cutler model [73] developed for the analysis of the compaction curves of fine-grained powders in a continuous heating regime. The Young–Cutler model [73] describes the initial stage of nonisothermic sintering of spherical particles in the conditions of simultaneous volume and grain boundary diffusion as well as plastic deformation processes. According to [73], the slope of the dependence $\ln(T\partial\varepsilon/\partial T) - T_m/T$ corresponds to the effective activation energy of the nonisothermic sintering process mQ_{s2} where m is a numerical coefficient depending on the diffusion mechanism and $T_m = T_{m(Ni)}$ = 1723 K is the melting point of the γ-phase [1,2]. Magnitudes of $m = 1/3$ were found for the case of the grain boundary diffusion, $m = 1/2$ were found for the case of the volume diffusion in the crystal lattice, and $m = 1$ were found for the case of the creep of the material [73].

The dependencies $\ln(T\cdot\partial\varepsilon/\partial T) - T_m/T$ are presented in Figure 14. As one can see in Figure 14, the dependencies $\ln(T\cdot\partial\varepsilon/\partial T) - T_m/T$ have a usual two-stage character that confirms the correctness of application of the Young–Cutler model to analyze the sintering kinetics of the W-Ni-Fe alloy. The values of the effective sintering activation energy at the intensive shrinkage stage (mQ_{s2}) are presented in Table 4. The mean uncertainty of determining the activation energy mQ_{s2} was $\pm 0.2\ kT_m$.

In the case of the coarse-grained powders, the magnitude of the effective SPS activation energy mQ_{s2} was close to the activation energy of the grain boundary diffusion in nickel ($Q_{b(Ni)}$ = 115 kJ/mol [72]) at $m = 1/3$. This suggests that the kinetics of high-speed sintering of the coarse-grained W-7%Ni-3%Fe powders at the intensive shrinkage stage is controlled by the intensity of the grain boundary diffusion in the γ-phase.

A good correspondence of the SPS activation energy of the nanopowders to the data on the activation energy of the diffusion processes reported in the literature was observed for $m = 1$ (Table 4). The value of $m = 1$ allows for concluding that the sintering kinetics of the W-7%Ni-3%Fe nanopowders is determined by the Coble creep intensity. This conclusion agrees qualitatively with M.F. Ashby's deformation-mechanism maps [72], in which the SPS regimes used in the present work correspond well to the creep area for nickel (stress $\sigma = 70\ MPa \sim 9\cdot10^{-4}\ G$ where G = 78.9 GPa [72] is the shear modulus for nickel, temperature 1200 °C). In our opinion, the large lengths of the grain boundaries in the sintered materials are the origin of the realization of the Coble creep mechanism in SPS of nanopowders since no intensive grain growth has taken place at this sintering stage yet. It is also notable that a decrease in the grain sizes would lead to an essential increase in the creep rate in the metal materials [74]. It is also notable that Coble creep is one of the main compaction mechanisms in SPS of WC [75], WC-Co [76,77], and YAG:Nd-W [78] nanopowders.

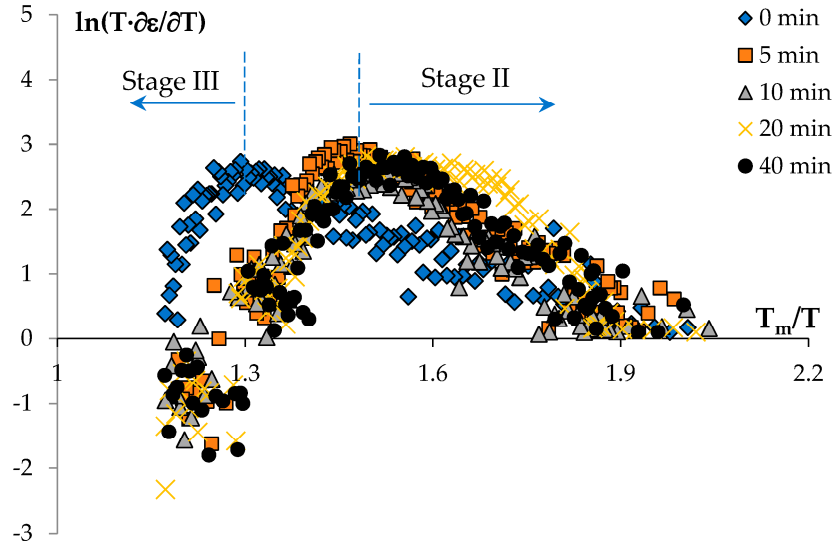


Figure 14. Dependencies $(T \cdot \partial\varepsilon/\partial T) - T_m/T$ for the W-7%Ni-3%Fe alloy. Analysis of the compaction mechanisms of the nonannealed nanopowders at Stage II.

It is notable that, sometimes, lower values of the activation energy of the grain boundary diffusion in fine-grained nickel are reported in the literature as well. In particular, creep activation energy of 110–115 kJ/mol and activation energy of the grain boundary diffusion of ~66 kJ/mol were reported for ultrafine-grained nickel with the grain sizes 0.3–0.5 μm [79].

The annealing of the nanopowders in hydrogen leads to a decrease in the SPS activation energy (Table 4). In our opinion, this originates from, first of all, the reduced concentration of oxygen adsorbed on the nanopowder particle surfaces. This leads to an increase in the diffusion creep rate in the W-7%Ni-3%Fe nanopowders at elevated temperatures. Thin tungsten oxide layers, which can form on the W nanoparticle surfaces when heating in vacuum, can be another origin of decreases in the creep rate. The oxide nanoparticles located at the tungsten grain boundaries can lead to a decrease in the creep rate at the second SPS stage.

In the high-temperature range, the slope of the dependence $\ln(T \cdot \partial\varepsilon/\partial T) - T_m/T$ (Figure 14) becomes negative. This means that one has to use another approach to estimate the sintering activation energy in a higher temperature range. According to [80], one can estimate the activation energy at this stage using the model of diffusion and dissolving of pores located near the grain boundaries in fine-grained materials. The correctness of application of this procedure was previously demonstrated in [47,78,81,82]. The activation energy at the nonisothermic sintering stage Q_{s3} can be determined from the slope of the dependence $\rho(T)/\rho_{th}$ in the double logarithmic axes $\ln(\ln(\alpha \cdot \rho/\rho_{th}/(1 - \rho/\rho_{th})) - T_m/T$ where α is the coefficient of compaction when pressing (α = 0.45 for nanopowders α-W) (Figure 15). The mean uncertainty in determining the activation energy Q_{s3} was $\pm 1.5\ kT_m$. The calculated values of Q_{s3} are presented in Table 4. For the annealed nanopowders, the value of Q_{s3} was ~2–3 kT_m lower than the one for the mechanically activated nanopowders.

The calculated values of the SPS activation energy are in good agreement with the activation energy of heterodiffusion of tungsten atoms in the γ-phase (taking into account corrections for a decrease in the activation energy of grain boundary diffusion in fine-grained materials [83]). Available data on the activation energy of the sintering of W-Ni-Fe alloys give completely different values; Q_s for the W-8.4Ni-3.6Fe alloy is 250 kJ/mol according to [84], while in [85] Q_s = 367 kJ/mol for the W-8.4Ni-3.6Fe alloy and 480 kJ/mol for 95W-3Ni-2Fe. It was shown in [86] that the activation energy of SPS for a fine-grained W-5.6%Ni-1.4%Fe alloy depends on the heating rate: at V < 30 °C/min, the value of Q_s = 454 kJ/mol, and at V > 200 °C/min the Q_s value = 200 kJ/mol. The diffusion activation

energy of ^{181}W in the nickel crystal lattice is Q_v ~268–309 kJ/mol [9,87]. In the cases of bulk diffusion in the Ni-W system and in the γ-Fe-W system, the Q_v values are 295–306 kJ/mol and 268 kJ/mol, respectively [88,89]. So far, it can be concluded that the compaction of W-Ni-Fe nanopowders at high temperatures is determined by the intensity of heterodiffusion of tungsten atoms in the crystal lattice of the γ-phase.

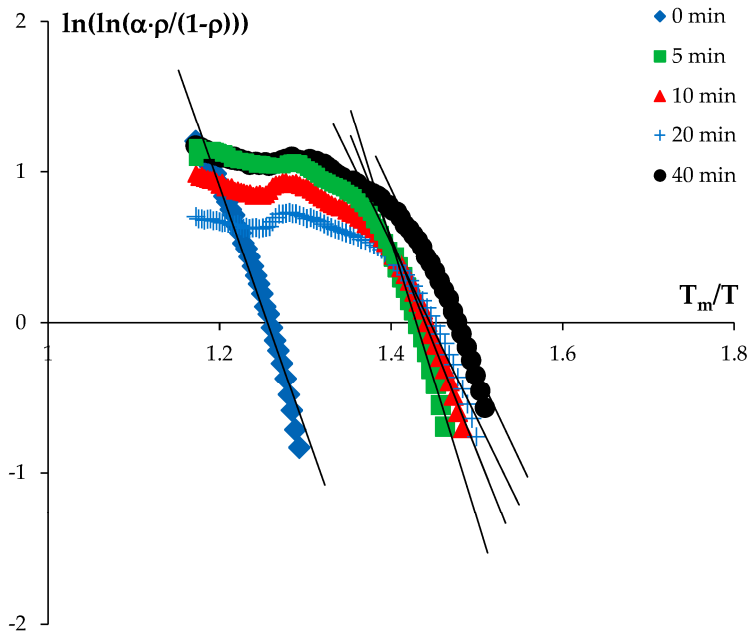


Figure 15. Dependencies $\ln(\ln(\alpha \cdot \rho/\rho_{th}/(1-\rho/\rho_{th})) - T_m/T$ for nonannealed W-7%Ni-3%Fe nanopowders.

Summarizing the results of this analysis, one should stress that intensive shrinkage of the mechanically activated W-7%Ni-3%Fe nanopowders occurs at low temperatures and is characterized by small values of compaction activation energy. In our opinion, low activation energy of sintering in nanopowder materials is the origin of the reduction in the activation energy of sintering for the W-Ni-Fe nanopowders.

According to the theory of nonequilibrium grain boundaries [83], the increase in the free (excess) volume of the grain boundaries Δα is the origin of the decrease in the activation energy of the grain boundary diffusion in strongly deformed fine-grained metals and alloys. The magnitude of Δα is proportional to the density of orientation mismatch dislocations (OMDs) captured by the grain boundaries during severe plastic deformation. In the course of HEBM, the grinding of the γ-phase particles with the FCC lattice is difficult due to the high ductility of these particles. In the course of HEBM, the grinding of the γ-phase particles and the accumulation of the OMDs at the grain boundaries take place [83]. The diffusion permeability of the γ-phase grain boundaries after HEBM appears to be higher than that of conventional grain boundaries in the γ-phase formed during sintering individual γ-phase particles to each other. The enhanced diffusion permeability of the nonequilibrium grain boundaries results in accelerated diffusion of the tungsten atoms in the γ-phase, and in an enhanced Coble creep rate. These factors lead to a decrease in the SPS activation energy of the W-Ni-Fe nanopowders.

The second factor promoting the decrease in the activation energy of the SPS of nanopowders can be the nonequilibrium state of their crystal lattice.

As has been shown above, an asymmetric distortion of the (110) α-W XRD peak towards higher reflection angles after HEBM was observed. In our opinion, this means that the crystal lattice constant in the surface layers of the W particles appears to be smaller than the one in the central parts of the W particles. So far, the asymmetry of the (110) α-W XRD peak originates from the increase in the concentrations of the Ni and Fe atoms in the

surface layers of the α-W particles and from the increase in the concentration of the W atoms in the γ-phase particles with nonequilibrium grain boundaries.

Tungsten is known to have high solubility in nickel. At elevated temperatures, the concentration of the W atoms in the γ-phase can reach 25–28% [4]. Partial dissolving of the α-W nanopowders in the γ-phase takes place during sintering, leading to a decrease in the density of the sintered W-Ni-Fe samples. This process can be accelerated by a larger specific surface area of the α-W nanoparticles, strong distortion of the crystal lattice in the surface layers of the α-W nanoparticles, and high diffusion permeability of the γ-phase nonequilibrium grain boundaries.

Now, we consider the origins of the nonmonotonous dependence of the density of the W-7%Ni-3%Fe alloy on the HEBM time (Figure 13). This effect was observed, in particular, for the nanopowders annealed in hydrogen and, consequently, its nature is not related to the oxidation of the nanopowders in the course of storing.

The primary origin of the decrease in the alloy density is the strain-stimulated dissolving of the W atoms in the γ-phase lattice during HEBM. This effect can have a considerable scale for the W-7%Ni-3%Fe alloy since the volume fraction of the γ-phase in this alloy exceeds 20%. Increasing the HEBM time leads to an increase in the volume fraction of the tungsten particles dissolved in the γ-phase. The decrease in the initial density of the W-Ni-Fe nanopowders would lead to a decrease in the final density of the alloy at given sintering regimes provided all other conditions are equal.

It is worth noting that the acceleration of the grain boundary diffusion processes and the increase in the creep rate should lead to an increase in the rate of solid phase sintering of the W-Ni-Fe nanopowders. This effect would compensate partly for the negative effect of HEBM on the density of the W-7%Ni-3%Fe alloy.

The question of the origins of the increase in the SPS activation energy and density with long HEBM times (t_{HEBM} = 40 min) is more complex. In our opinion, this effect is caused simultaneously by three factors.

First, it is worth noting that the intensity of the strain-induced dissolving of the tungsten particles can decrease at long HEBM times due to the achievement of the solubility limit of W in the γ-phase. In this case, the increase in the HEBM time leads to an increase in the creep rate due to an increase in the nonequilibrium degree of the grain boundaries in the γ-phase and a decrease in the grain sizes in the alloy. This should help increase the density of tungsten alloys.

The XRD phase analysis shows that the microstrain of the α-W crystal lattice begins to decrease after 40 min of HEBM (Figure 5b). This effect can originate from the decrease in the concentrations of the Ni and Fe atoms in the surface layers of the α-W nanoparticles as well as from the decrease in the dislocation density in the α-W particles. The heating of the powders during HEBM is the most probable origin of this effect. The increase in the temperature during HEBM reduces the distortion degree of the α-W crystal lattice and, as a consequence, the tendency of the nanoparticles to dissolve in the strongly deformed γ-phase. This leads to an increase in the density of the tungsten alloy.

The increase in the density of agglomerates after 40 min of HEBM is the third probable origin. The increase in the density of agglomerates can originate from the intensive plastic deformation of the tungsten nanoparticles during HEBM as well as from the heating of the samples. The increase in the packing density of the nanoparticles inside the agglomerates leads to an increase in the initial density of the powder composition W-Ni-Fe and, as a consequence, provides an opportunity to achieve a higher final density of the tungsten alloy when sintering in the same conditions.

Finally, we will discuss briefly the results of investigations into the mechanical properties of the HTAs. As one can see in Figure 16a, the dependencies of hardness and yield strength on the grain size can be described by the Hall–Petch relation with good accuracy. Traditionally, the dependence of the strength characteristics on the grain size in coarse-grained HTAs is suggested to have more complex character. In particular, the magnitudes of the ultimate strength and of the yield strength in the tension tests depend strongly on

the volume fraction of the γ-phase particles as well as on the relations of the lengths of the intergranular boundaries W-W and those of the interphase boundaries W-γ [5,12,32,33]. The realization of the Hall–Petch effect in ultrafine-grained HTAs can be a consequence of considerably greater lengths of grain boundaries that lead to a proportional decrease in the sizes (thicknesses) of the interphase boundaries α-W-γ-phase.

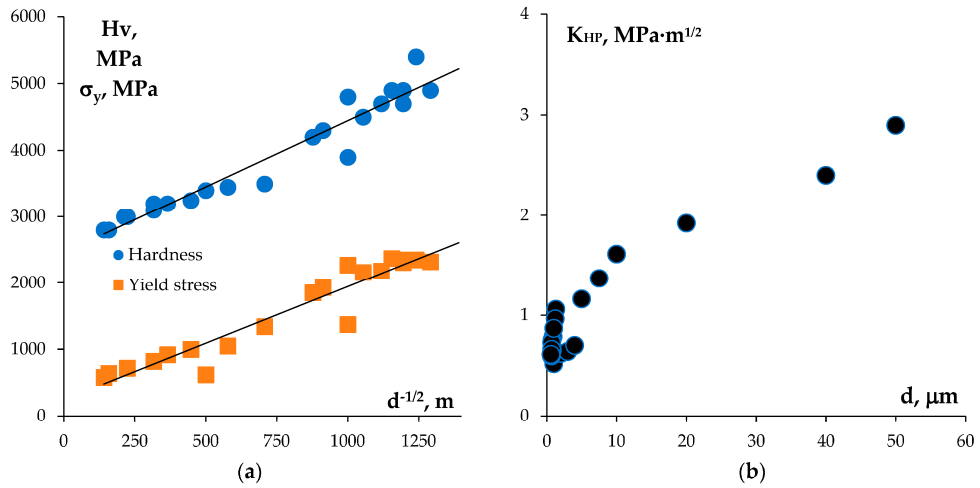


Figure 16. Analysis of investigations of the mechanical properties of the HTAs 90%W-7%Ni-3%Fe: (**a**) dependencies of the hardness and of the yield strength on the grain size; (**b**) dependence of Hall–Petch coefficient on the grain size. Analysis of the results presented in Tables 2 and 3.

Knowing the magnitudes of the yield strength σ_y, of the macroelasticity stress σ_0, and of the average grain size d, one can calculate the Hall–Petch coefficient according to the formula $K_{HP} = (\sigma_y - \sigma_0) \cdot d^{1/2}$ for each alloy, as reflected in Tables 2 and 3. Figure 16b presents the dependence of K_{HP} on the grain size. As one can see in Figure 16b, increasing the sintering temperature and the grain growth led to an increase in the Hall–Petch coefficient. The maximum magnitudes of K_{HP} were achieved in the HTAs sintered at 1450 and 1500 °C (Table 2). In our opinion, this evidences an increase in the adhesion strength of the interphase boundaries with increasing sintering temperature. The increase in the concentration of the W atoms in the γ-phase can also contribute additionally to the increase in K_{HP}.

No essential differences in the magnitudes of K_{HP} for the alloys obtained from the nonannealed and annealed nanopowders were observed. This suggests that the differences in the strength characteristics of the HTAs are observed to originate from, first of all, the differences in the grain sizes.

5. Conclusions

1. High-energy ball milling (HEBM) of W-Ni-Fe powders leads to grinding of the tungsten particles and to the formation of a supersaturated solid solution of W atoms in the γ-phase. After HEBM, the W nanoparticles have core–shell structures, which have high concentrations of Ni and Fe atoms in the surface layers of the α-W nanoparticles. This leads to broadening and asymmetry of the α-W XRD peaks.
2. The SPS kinetics for the initial fine W-7%Ni-3%Fe powders is governed by the intensity of grain boundary diffusion in the γ-phase. SPS was shown to allow obtaining samples with increased density, small grain sizes (~1.2–1.3 μm), and increased hardness (4.2–4.3 GPa) as compared with the samples obtained via conventional sintering of the fine-grained powders in hydrogen.
3. The SPS kinetics of the nanopowders has a two-stage character owing to intensive Coble diffusion creep in the low-temperature range and intensive diffusion of W atoms in the crystal lattice of the γ-phase at elevated temperatures. The SPS activation energy in the low heating temperature range is small and originates from the nonequilibrium state of the grain boundaries in the γ-phase with an increased density of defects arising

during HEBM. The recrystallization process in the γ-phase is a possible origin of the change in the diffusion mechanism responsible for the intensity of the nanopowder compaction process in SPS. Reducing the activation energy of sintering will improve the density of the sintered samples.

4. The relative density of HTAs obtained using SPS was shown to depend on the HEBM time non-monotonously (with a minimum). It was suggested that the effect of the reduction in the density is caused by the formation of strongly supersaturated solid solutions of Ni and Fe in the tungsten particles. Increasing the HEBM time leads to a decrease in particle size and an increase in the diffusion coefficient across nonequilibrium grain boundaries. This will contribute to an increase in the creep rate and acceleration of sintering of HTAs, and, as a consequence, will lead to an increase in the density of HTAs.
5. Annealing the nanopowders in hydrogen was shown to result in a decrease in the sintering activation energy and in an increase in the density of the sintered HTAs. This originates from the decrease in the oxygen concentration in the nanopowders and an increase in the Coble diffusion creep rate in SPS.
6. The dependencies of the yield strength and of the hardness on the grain size are described by the Hall–Petch equation with good accuracy. The maximum values of the Hall–Petch coefficient were observed for the alloys sintered in hydrogen at elevated temperatures (1450, 1500 °C). This originates from the high adhesion strength of the interphase boundaries and probably also from the increased concentration of W atoms in the γ-phase.

Author Contributions: Conceptualization, N.V.M. (Nataliya V. Malekhonova) and A.V.N.; methodology, N.V.M. (Nataliya V. Malekhonova) and A.V.N.; formal analysis, N.V.M. (Nataliya V. Malekhonova), V.N.C. and A.V.N.; investigation, N.V.M. (Nataliya V. Malekhonova), N.V.M. (Nikolay V. Melekhin), A.M.B., A.R.F., M.S.B., E.A.L. and N.V.S.; resources, V.N.C.; data curation, N.V.M. (Nataliya V. Malekhonova) and A.V.N.; writing—original draft preparation, N.V.M. (Nataliya V. Malekhonova), V.N.C. and A.V.N.; writing—review and editing, N.V.M. (Nataliya V. Malekhonova), V.N.C. and A.V.N.; visualization, N.V.M. (Nataliya V. Malekhonova) and A.V.N.; supervision, V.N.C.; project administration, N.V.M. (Nataliya V. Malekhonova); funding acquisition, N.V.M. (Nataliya V. Malekhonova). All authors have read and agreed to the published version of the manuscript.

Funding: This research was funded by the Russian Science Foundation (grant number 22-79-10080) and Ministry of Science and Higher Education of the Russian Federation (project H-498-99_2021-2023 of Federal Academic Leadership Program Priority-2030).

Data Availability Statement: Not applicable.

Conflicts of Interest: The authors declare no conflict of interest.

Abbreviations

LPS—conventional liquid-phase sintering; CG—coarse-grained (alloy); GB—grain boundary; CSR—coherent scattering regions; HTA—heavy tungsten alloy; HEBM—high-energy ball milling; OMDs—orientation mismatch dislocations; SEM—scanning electron microscopy; SPS—spark plasma sintering; UFG—ultrafine-grained (alloy); XRD—X-ray diffraction (phase analysis); V—heating rate; T—sintering temperature; t_s—holding time at sintering temperature; T_m—melting point; G—shear modulus; t_{HEBM}—HEBM time; ρ—density; ρ_{th}—theoretical density; d—average grain size; D_{XRD}—sizes of coherent scattering regions; σ_0—macroelasticity stress (lattice friction stress); σ_y—yield strength; H—depth of sample embedding into steel target; Hv—Vickers hardness; Ys—dynamic yield strength; K_{HP}—Hall–Petch coefficient; L—shrinkage; L_{max}—maximum shrinkage; S—shrinkage rate; S_{max}—maximum shrinkage rate; Q_s—activation energy of sintering; Q_v—activation energy of volume diffusion; Q_b—activation energy of grain boundary diffusion; α—coefficient of compaction when pressing; m—numerical coefficient for the Young–Cutler model; ε—relative shrinkage in the Young–Cutler model; Δε—microstrain of the tungsten crystal lattice.

Appendix A

Table A1. Microstructure parameters and mechanical properties of HTAs obtained with SPS/FAST.

Ref.	Alloy (wt.%)	SPS Modes				Characteristics of the HTA			Note [2]
		T_s, °C	V, °C/min	P, MPa	t_s, min	Density (ρ)	d, μm	Mechanical Properties [1]	
[23]	W-4Ni-2Co-1Fe	1200–1400	-	30	6	16.78 g/cm^3	0.34	84.3 HRA σ_{ts} = 968 MPa	R_0 = 120 nm t_{HEBM} = 15 h, 226 r/min
[24]	W-5.6Ni-1.4Fe	1230	90	50	0	16.3 g/cm^3 (~92%)	0.72	No data	R_0 = 6 nm t_{HEBM} = 40 h, 226 rpm. Add: Ni_2W_4C, Fe_6W_6C
[25]	W-5.6Ni-1.4Fe	1410	90	30	0	99.4%	~2	No data	R_0 = 2.44 μm
[26]	W-5.6Ni-1.4Fe	1360	380	30	0	94.8%	6.0	σ_y = 1050 MPa σ_b = 1580 MPa 418 HV_1	R_0 = 2.44 μm
[27]	W-5.6Ni-1.4Fe	1400	105	30	2	~98%	4.4	σ_b = 1700 MPa 418 HV_1	-
		+ cyclic heat treatment at 1400 °C				~98%	~6	σ_b = 1780 MPa 489 HV_1	
[28]	W-7Ni-3Fe	1150	100	50	8	96.12%	5–10	σ_b = 1020 MPa 68–69 HRA	R_0 = 1–3 μm [3] t_{HEBM} = 5 h, 266 rpm. Add: WC, NiW
[29]	W-5.6Ni-1.4Fe	1320	90	30	0–45	~96%	4–7	No data	R_0 = 2.44 μm
[30]	W-2Mo-7Ni-3Fe	1200	100	50	8	96.42%	4–5	σ_b = 922 MPa 73.8 HRA	R_0 = 1–3 μm [3] t_{HEBM} = 40 h, 800 rpm. Add: NiW, Ni_2W_4C, WC
[31]	W-8Ni-2Fe	1000	100	30	0	80.84%	10–20	σ_y = 586 MPa σ_b = 975 MPa 63 HRA	D_{90} = 6.3 μm [3] t_{HEBM} = 40 h, 260 rpm
	W-8Ni-2Fe-6Mo					84.61%	5–20	σ_y = 784 MPa σ_b = 1025 MPa 65 HRA	
	W-8Ni-2Fe-12Mo					86.34%	10–20	σ_y = 825 MPa σ_b = 1120 MPa 68 HRA	
	W-8Ni-2Fe-18Mo					93.12%	10–20	σ_y = 950 MPa σ_b = 1160 MPa 72 HRA	
	W-8Ni-2Fe-24Mo					94.25%	15–20	σ_y = 998 MPa σ_b = 1250 MPa 75 HRA	
[32]	W-7Ni-3Fe	1100	100	30	2	68.57%	11.45	σ_y = 475 MPa 138 $HV_{0.5}$	D_{90} = 6.2 μm [3] t_{HEBM} = 30 min (in the mortar)
	W-7Ni-3Fe-0.25La_2O_3					87.95%	10.66	σ_y = 497 MPa 357 $HV_{0.5}$	
	W-7Ni-3Fe-0.50La_2O_3					76.83%	9.76	σ_y = 822 MPa 370 $HV_{0.5}$	
	W-7Ni-3Fe-0.755La_2O_3					75.51%	8.88	σ_y = 952 MPa 397 $HV_{0.5}$	
	W-7Ni-3Fe-1La_2O_3					70.44%	7.89	σ_y = 1110 MPa 533 $HV_{0.5}$	
[33]	W-7Ni-3Fe-0.5SiC	1400	100	50	5	93.95%	10–20	σ_y = 1068 MPa 443 $HV_{0.5}$	R_0 = 10 μm [3] t_{HEBM} = 1 h + pressed 600 MPa
	W-7Ni-3Fe-1SiC					90.98%	5–20	σ_y = 810 MPa 458 $HV_{0.5}$	
	W-7Ni-3Fe-1.5SiC					85.05%	5–20	σ_y = 708 MPa 532 $HV_{0.5}$	
	W-7Ni-3Fe-2SiC					82.86%	5–10	σ_y = 729 MPa 564 $HV_{0.5}$	

Table A1. *Cont.*

Ref.	Alloy (wt.%)	SPS Modes				Characteristics of the HTA			Note [2]
		T_s, °C	V, °C/min	P, MPa	t_s, min	Density (ρ)	d, μm	Mechanical Properties [1]	
[34]	W-7Ni-3Fe	1000	100	50	8	~93%	<1	σ_y = 954.5 MPa 79.3 HRA	R_0 = 2.3–2.7 μm [3] t_{HEBM} = 40 h, 266 rpm
		1250				~87%	3–5	σ_y = 353.6 MPa 63.8 HRA	
[35]	W-2Mo-6Ni-2.5Fe-1.5Co	1000	100	50	8	90.68%	~2	σ_b = 595 MPa 76.14 HRA	R_0 = 1–3 μm [3] t_{HEBM} = 20 h, 220 rpm
		1250				98.93%	5.4	σ_b = 1040 MPa 71.43 HRA	
[36]	W-5.6Ni-2.4Fe	1400	100	30	-	~84.8%	12.3	σ_y = 686 MPa σ_t = 975 MPa 385 $HV_{0.5}$	R_0 = 10 μm [3] t_{HEBM} = 1 h Add: Ni-W
	W-5.6Ni-2.4Fe-0.5Co					93.365	11.56	σ_y = 770 MPa σ_t = 961 MPa 455 $HV_{0.5}$	
	W-5.6Ni-2.4Fe-1Co					~90.5%	9.48	σ_y = 1300 MPa σ_t = 1508 MPa 467 $HV_{0.5}$	
	W-5.6Ni-2.4Fe-1.5Co					~87%	9.68	σ_y = 1080 MPa σ_t = 1330 MPa 471 $HV_{0.5}$	
	W-5.6Ni-2.4Fe-2Co					~83%	11.1	σ_y = 1000 MPa σ_t = 1256 MPa 499 $HV_{0.5}$	
[37]	W-21Ni-9Fe	1250	100	40	4	98.6	~10	σ_t = 890 MPa 25.6 HRC	t_{HEBM} = 4 h, 400 rpm
[38]	W-5.6Ni-1.4Fe	1050–1100	100	50	5	98.12	0.871	σ_b = 987 MPa 84.3 HRA	R_0 = 100 nm [3] t_{HEBM} = 6 h, 300 rpm
[39]	W-2Mo-7Ni-3Fe	1150	100	50	8	No data	~2	σ_b = 390.1 MPa 69–70 HRA	R_0 = 1–3 μm [3] t_{HEBM} = 40 h, 266 rpm Add: Ni_2W_4C

[1] σ_{ts}—transverse rupture strength, σ_b—bending strength, σ_y—yield strength, σ_t—tensile strength. [2] R_0 is the initial particle size; Add—there are auxiliary phases in the specimens. [3] The initial particle size of the α-W.

References

1. Green, E.C.; Jones, D.J.; Pitkin, W.R. Developments in high-density alloys. *Proc. Symp. Powder Metall.* **1954**, *58*, 253–256.
2. Krock, R.; Shepard, H. Mechanical behavior of the two-phase composite tungsten-nickel-iron. *Trans. Metall. Soc. AIME* **1963**, *227*, 1127–1134.
3. Das, J.; Rao, G.A.; Pabi, S.K. Microstructure and mechanical properties of tungsten heavy alloys. *Mater. Sci. Eng. A* **2010**, *527*, 7841–7847. [CrossRef]
4. Povarova, K.B.; Makarov, P.V.; Ratner, A.D.; Zavarzina, E.K.; Volkov, K.V. VNZH-90-type heavy alloys. I. Effect of alloying and the conditions of fabricating tungsten powders on their structure and the properties of sintered alloys. *Russ. Metall.* **2002**, *4*, 39–48. (In Russian)
5. Sahin, Y. Recent progress in processing of tungsten heavy alloys. *J. Powder Technol.* **2014**, *2014*, 764306. [CrossRef]
6. Ishchenko, A.N.; Afanas'eva, S.A.; Belov, N.N.; Burkin, V.V.; Galsanov, S.V.; Kasimov, V.Z.; Kudryavtsev, V.A.; Lipatnikova, Y.D.; Martsunova, L.S.; Rogaev, K.S.; et al. Destruction features of impactors made of a porous alloy based on tungsten with reinforcing filler when interacting with armored obstacles. *Tech. Phys.* **2020**, *65*, 414–419. [CrossRef]
7. Luo, R.; Huang, D.; Yang, M.; Tang, E.; Wang, M.; He, L. Penetrating performance and "self-sharpening" behavior of fine-grained tungsten heavy alloy rod penetrators. *Mater. Sci. Eng. A* **2016**, *675*, 262–270. [CrossRef]
8. German, R.M. Sintered tungsten heavy alloys: Review of microstructure, strength, densification, and distortion. *Int. J. Refract. Met. Hard Mater.* **2022**, *108*, 105940. [CrossRef]
9. Ravi Kiran, U.; Panchal, A.; Sankaranarayana, M.; Nandy, T.K. Tensile and impact behavior of swaged tungsten heavy alloys processed by liquid phase sintering. *Int. J. Refract. Met. Hard Mater.* **2013**, *37*, 1–11. [CrossRef]
10. Ravi Kiran, U.; Sambasiva Rao, A.; Sankaranarayana, M.; Nandy, T.K. Swaging and heat treatment studies on sintered 90W-6Ni-2Fe-2Co tungsten heavy alloy. *Int. J. Refract. Met. Hard Mater.* **2012**, *33*, 113–121. [CrossRef]
11. Gong, X.; Fan, J.L.; Ding, F.; Song, M.; Huang, B.Y.; Tian, J.M. Microstructure and highly enhanced mechanical properties of fine-grained tungsten heavy alloy after one-pass rapid hot extrusion. *Mater. Sci. Eng. A* **2011**, *528*, 3646–3652. [CrossRef]

12. Yu, Y.; Zhang, W.; Chen, Y.; Wang, E. Effect of swaging on microstructure and mechanical properties of liquid-phase sintered 93W-4.9(Ni,Co)-2.1Fe alloy. *Int. J. Refract. Met. Hard Mater.* **2014**, *44*, 103–108. [CrossRef]
13. Das, J.; Kiran, U.R.; Chakraborty, A.; Prasad, N.E. Hardness and tensile properties of tungsten based heavy alloys prepared by liquid phase sintering technique. *Int. J. Refract. Met. Hard Mater.* **2009**, *27*, 577–583. [CrossRef]
14. Mazilkin, A.A.; Straumal, B.B.; Protasova, S.G.; Bulatov, M.F.; Baretzky, B. Pseudopartial wetting of W/W grain boundaries by the nickel-rich layers. *Mater. Lett.* **2017**, *192*, 101–103. [CrossRef]
15. Luo, J.; Gupta, V.K.; Yoon, D.H.; Meyer, H.M. Segregation-induced grain boundary premelting in nickel-doped tungsten. *Appl. Phys. Lett.* **2005**, *87*, 231902. [CrossRef]
16. Fortuna, E.; Sikorsky, K.; Kurzydlowski, K.J. Experimental studies of oxygen and carbon segregation at the interfacial boundaries of a 90W-7Ni-3Fe tungsten heavy alloy. *Mater. Charact.* **2004**, *52*, 323–329. [CrossRef]
17. Krasovskii, P.V.; Samokhin, A.V.; Fadeev, A.A.; Sinayskiy, M.A.; Sigalev, S.K. Alloying effects and composition inhomogeneity of plasma-created multimetallic nanopowders: A case study of the W-Ni-Fe ternary system. *J. Alloys Compd.* **2018**, *250*, 265–275. [CrossRef]
18. Parabhu, G.; Kumar, N.A.; Sankaranarayana, M.; Nandy, T.K. Tensile and impact properties of microwave sintered tungsten heavy alloys. *Mater. Sci. Eng. A* **2014**, *607*, 63–70. [CrossRef]
19. Gryaznov, M.; Samokhin, A.; Chuvil'deev, V.; Fadeev, A.; Alekseev, N.; Shotin, S.; Dorofeev, A.; Zavertyaev, A. Method of W-Ni-Fe composite spherical powder production and the possibility of its application in Selective Laser Melting technology. *Metals* **2022**, *12*, 1715. [CrossRef]
20. Chen, H.; Ye, L.; Han, Y.; Chen, C.; Fan, J. Additive manufacturing of W-Fe composites using laser metal deposition: Microstructure, phase transformation, and mechanical properties. *Mater. Sci. Eng. A* **2021**, *811*, 141036. [CrossRef]
21. Chen, H.; Zi, X.; Han, Y.; Dong, J.; Liu, S.; Chen, C. Microstructure and mechanical properties of additive manufactured W-Ni-Fe-Co composite produced by selective laser melting. *Int. J. Refract. Met. Hard Mater.* **2020**, *86*, 105111. [CrossRef]
22. Liu, W.; Ma, Y.; Zhang, J. Properties and microstructural evolution of W-Ni-Fe alloy via microwave sintering. *Int. J. Refract. Met. Hard Mater.* **2012**, *35*, 138–142. [CrossRef]
23. Han, Y.; Wu, X.; Jiang, X.; Yang, Y. Powder extrusion printing and sintering densification behaviors of ultrafine 98W-1Ni-1Fe alloy powder. *Crystals* **2022**, *12*, 875. [CrossRef]
24. Tokita, M. Progress of Spark Plasma Sintering (SPS): Method, Systems, Ceramics Applications and Industrialization. *Ceramics* **2021**, *4*, 160–198. [CrossRef]
25. Mukasyan, A.S.; Rogachev, A.S.; Moskovskikh, D.O.; Yermekova, Z.S. Reactive spark plasma sintering of exothermic systems: A critical review. *Ceram. Int.* **2022**, *48*, 2988–2998. [CrossRef]
26. Munir, Z.A.; Anselmi-Tamburini, U.; Ohyanagi, M. The effect of electric field and pressure on the synthesis and consolidation materials: A review of the spark plasma sintering method. *J. Mater. Sci.* **2006**, *41*, 763–777. [CrossRef]
27. Olevsky, E.; Dudina, D. *Field-Assisted Sintering*; Springer Int. Publ.: Berlin/Heidelberg, Germany, 2018. [CrossRef]
28. Chuvildeev, V.N.; Panov, D.V.; Boldin, M.S.; Nokhrin, A.V.; Blagoveshchensky, Y.V.; Sakharov, N.V.; Shotin, S.V.; Kotkov, D.N. Structure and properties of advanced materials obtained by Spark Plasma Sintering. *Acta Astronaut.* **2015**, *109*, 172–176. [CrossRef]
29. Li, X.; Xin, H.; Hu, K.; Li, Y. Microstructure and properties of ultra-fine tungsten heavy alloys prepared by mechanical alloying and electric current activated sintering. *Trans. Nonferrous Met. Soc. China* **2010**, *20*, 443–449. [CrossRef]
30. Hu, K.; Zheng, D.; Li, Y. SPS densification behavior of W-5.6Ni-1.4Fe heavy alloy powders. *Rare Met.* **2011**, *30*, 581–587. [CrossRef]
31. Hu, K.; Li, X.-q.; Yang, C.; Li, Y.-y. Densification and microstructure evolution during SPS consolidation process in W-Ni-Fe system. *Trans. Nonferrous Met. Soc. China* **2011**, *21*, 493–501. [CrossRef]
32. Li, Y.; Hu, K.; Li, X.; Qu, S. Fine-grained 93W-5.6Ni-1.4Fe heavy alloys with enhanced performance prepared by spark plasma sintering. *Mater. Sci. Eng. A* **2013**, *573*, 245–252. [CrossRef]
33. Li, X.; Hu, K.; Qu, S.; Yang, C. 93W-5.6Ni-1.4Fe heavy alloys with enhanced performance prepared by cyclic spark plasma sintering. *Mater. Sci. Eng. A* **2014**, *599*, 233–241. [CrossRef]
34. Xiang, D.P.; Ding, L.; Li, Y.Y.; Chen, G.B.; Zhao, Y.W. Preparation of fine-grained tungsten heavy alloys by spark plasma sintered W-7Ni-3Fe composite powders with different ball milling time. *J. Alloys Compd.* **2013**, *562*, 19–24. [CrossRef]
35. Hu, K.; Li, X.; Qu, S.; Li, Y. Spark-Plasma Sintering of W-5.6Ni-1.4Fe heavy alloys: Densification and grain growth. *Metall. Mater. Trans. A* **2013**, *44*, 923–933. [CrossRef]
36. Xiang, D.P.; Ding, L.; Li, Y.Y.; Chen, X.Y.; Zhang, T.M. Fabricating fine-grained tungsten heavy alloy by spark plasma sintering of low-energy ball-milled W-2Mo-7Ni-3Fe powders. *Mater. Sci. Eng. A* **2013**, *578*, 18–23. [CrossRef]
37. Prasad, B.S.L.; Annamalai, R. A study of molybdenium addition on W-Ni-Fe based heavy alloys sintered with spark plasma sintering. Bulletin of the Polish Academy of Science. *Tech. Sci.* **2019**, *67*, 167–172. [CrossRef]
38. AyyappaRaj, M.; Yadav, D.; Agrawal, D.K.; Rajan, R.A.A. Microstructure and mechanical properties of spark plasma-sintered La2O3 dispersion-strengthened W-Ni-Fe alloy. *Rare Metals* **2020**, *40*, 2230–2236. [CrossRef]
39. Chaurasia, J.K.; Muthuchamy, A.; Patel, P.N.; Annamalai, A.R. Densification of SiC particle reinforced W-Ni-Fe heavy alloy composites through conventional and Spark Plasma Sintering. *Trans. Indian Inst. Met.* **2017**, *70*, 2185–2191. [CrossRef]
40. Ding, L.; Xiang, D.P.; Li, Y.Y.; Li, C.; Li, J.B. Effects of sintering temperature on fine-grained tungsten heavy alloy produced by high-energy ball milling assisted spark plasma sintering. *Int. J. Refract. Met. Hard Mater.* **2012**, *33*, 65–69. [CrossRef]

41. Ding, L.; Xiang, D.P.; Pan, Y.L.; Li, Y.Y. Mechanical properties and microstructural evolution of Mo-Co-co-strengthened W-Ni-Fe alloys by spark plasma sintering. *J. Alloys Compd.* **2017**, *712*, 593–598. [CrossRef]
42. Senthilnathan, N.; Raja Annamalai, A.; Venkatachalam, G. Microstructure and mechanical properties of spark plasma sintered tungsten heavy alloys. *Mater. Sci. Eng. A* **2018**, *710*, 66–73. [CrossRef]
43. Wu, Y.; Li, Y.; Yu, D. Fine-grained W-Ni-Fe heavy alloys prepared by Spark Plasma Sintering. *Mater. Sci. Forum* **2016**, *849*, 745–752. [CrossRef]
44. Jingang, Z.; Weimin, W.; Wei, J.; Qianglong, H.; Aiang, W.; Lin, T.; Kai, Y. Ultrafine grain tungsten heavy alloys with excellent performance prepared by Spark Plasma Sintering. *J. Wuhan Univ. Technol. Mater. Sci. Ed.* **2020**, *35*, 393–398. [CrossRef]
45. Ding, L.; Xiang, D.P.; Li, Y.Y.; Zhao, Y.W.; Li, J.B. Phase, microstructure and properties evolution of fine-grained W-Mo-Ni-Fe alloy during spark plasma sintering. *Mater. Des.* **2012**, *37*, 8–12. [CrossRef]
46. Zhang, F.L.; Wang, C.Y.; Zhu, M. Nanostructured WC/Co composite powder prepared by high energy ball milling. *Scr. Mater.* **2003**, *49*, 1123–1128. [CrossRef]
47. Suryanarayana, C. Mechanical alloying and milling. *Prog. Mater. Sci.* **2001**, *46*, 1–184. [CrossRef]
48. Jing-lian, F.; Tao, L.; Hui-chao, C.; Deng-long, W. Preparation of fine grain tungsten heavy alloy with high properties by mechanical alloying and yttrium oxide addition. *J. Mater. Process. Technol.* **2008**, *208*, 463–469. [CrossRef]
49. Liang, Y.X.; Wu, Z.M.; Fu, E.G.; Du, J.L.; Wang, P.P.; Zhao, Y.B.; Qiu, Y.H.; Hu, Z.Y. Refinement process and mechanisms of tungsten powder by high energy ball milling. *Int. J. Refract. Met. Hard Mater.* **2017**, *67*, 1–8. [CrossRef]
50. Hu, W.; Dong, Z.; Yu, L.; Ma, Z.; Liu, Y. Synthesis of W-Y_2O_3 alloys by freeze-drying and subsequent low temperature sintering: Microstructure refinement and second phase particles regulation. *J. Mater. Sci. Technol.* **2020**, *36*, 84–90. [CrossRef]
51. Dong, Z.; Liu, N.; Ma, Z.; Liu, C.; Guo, Q.; Liu, Y. Preparation of ultra-fine grain W-Y_2O_3 alloy by an improved wet chemical method and two-step spark plasma sintering. *J. Alloys Compd.* **2017**, *695*, 2969–2973. [CrossRef]
52. Wu, C. Preparation of ultrafine tungsten powders by in-situ hydrogen reduction of nano-needle violet tungsten oxide. *Int. J. Refract. Met. Hard Mater.* **2011**, *29*, 686–691. [CrossRef]
53. Seegopaul, P.; McCandlish, L.E.; Shinneman, F.M. Production capability and powder processing methods for nanostructured WC-Co powder. *Int. J. Refract. Met. Hard Mater.* **1997**, *15*, 133–138. [CrossRef]
54. Lassner, E.; Schubert, W.D. *Tungsten: Properties, Chemistry, Technology of the Elements, Alloys, and Chemical Compounds*; Springer Science & Business Media: Berlin/Heidelberg, Germany, 1999.
55. Malewar, R.; Kumar, K.S.; Murty, B.S.; Sarma, B.; Pabi, S.K. On sinterability of nanostructured W produced by high-energy ball milling. *J. Mater. Res.* **2007**, *22*, 1200–1206. [CrossRef]
56. De Castro, C.L.; Mitchell, B.S. The use of polymeric milling media in the reduction of contamination during mechanical attrition. *J. Mater. Res.* **2002**, *17*, 2997–2999. [CrossRef]
57. Kiran, U.R.; Kumar, M.P.; Sankaranarayana, M.; Singh, A.K.; Nandy, T.K. High energy milling on tungsten powders. *Int. J. Refract. Met. Hard Mater.* **2015**, *48*, 74–81. [CrossRef]
58. Han, Y.; Fan, J.; Liu, T.; Cheng, H.; Tian, J. The effects of ball-milling treatment on the densification behavior of ultra-fine tungsten powder. *Int. J. Refract. Met. Hard Mater.* **2011**, *29*, 743–750. [CrossRef]
59. Malkin, A.I.; Fomkin, A.A.; Klyuev, V.A.; Loznetsova, N.N.; Popov, D.A.; Toporov, Y.P.; Shkolin, A.V. The influence of mechanical activation on the adsorption properties of powdered tungsten. *Prot. Met. Phys. Chem. Surf.* **2015**, *51*, 81–84. [CrossRef]
60. Malkin, A.I.; Kiselev, M.R.; Klyuev, V.A.; Loznetsova, N.N.; Toporov, Y.P. The effect of mechanical activation on the heat capacity of powdered tungsten. *Tech. Phys. Lett.* **2012**, *38*, 509–510. [CrossRef]
61. Savenko, V.I.; Toropov, Y.P.; Chernyshev, V.V.; Malkin, A.I. Microstructure and properties of surface-modified tungsten powders mechanically activated in different media. *Phys. Met. Metallogr.* **2017**, *118*, 1066–1072. [CrossRef]
62. Chuvil'deev, V.N.; Nokhrin, A.V.; Boldin, M.S.; Baranov, G.V.; Sakharov, N.V.; Belov, V.Y.; Lantsev, E.A.; Popov, A.A.; Melekhin, N.V.; Lopatin, Y.G.; et al. Impact of mechanical activation on sintering kinetics and mechanical properties of ultrafine-grained 95W-Ni-Fe tungsten heavy alloys. *J. Alloys Compd.* **2019**, *773*, 666–688. [CrossRef]
63. Bragov, A.M.; Chuvil'deev, V.N.; Melekhin, N.V.; Filippov, A.R.; Konstantinov, A.Y.; Sakharov, N.V. Dynamic strength of heavy 90W-7Ni-3Fe alloy produced by Spark Plasma Sintering. *Phys. Mesomech.* **2019**, *22*, 307–312. [CrossRef]
64. Dudina, D.V.; Bokhonov, B.B.; Ukhina, A.V.; Anisimov, A.G.; Mali, V.I.; Esikov, M.A.; Batraev, I.S.; Kuznechik, O.O.; Pilinevich, L.P. Reactivity of materials towards carbon of graphite foil during Spark Plasma Sintering: A case study using Ni-W powders. *Mater. Lett.* **2016**, *168*, 62–67. [CrossRef]
65. Bokhonov, B.B.; Ukhina, A.V.; Dudina, D.V.; Anisimov, A.G.; Mali, V.I.; Batraev, I.S. Carbon uptake during Spark Plasma Sintering: Investigation through the analysis of the carbide "footprint" in a Ni-W alloy. *RSC Adv.* **2015**, *98*, 80228–80237. [CrossRef]
66. Williamson, G.K.; Hall, W.M. X-ray line broadening from aluminium and wolfram. *Acta Metall.* **1953**, *1*, 22–31. [CrossRef]
67. Kolsky, H. An investigation of the mechanical properties of materials at very high rates of loading. *Proc. Phys. Society. Sect. B* **1949**, *62*, 676–700. [CrossRef]
68. Duan, B.; Zhou, T.; Yang, G.; Yang, D.; Wang, D. Microstructures and properties of 90W-4Ni-6Mn alloy prepared by vacuum sintering. *Mater. Res. Express* **2020**, *7*, 036522. [CrossRef]
69. Farooq, S.; Kemp, P.B.; German, R.M.; Base, A. Effect of initial oxygen content and sintering atmosphere dew point on the properties of tungsten based heavy alloys. *Int. J. Refract. Met. Hard Mater.* **1989**, *8*, 236–243.
70. Rahaman, M.N. *Ceramic Processing and Sintering*; CRC Press: Boca Raton, FL, USA, 2017; Volume 1.

71. Wang, J.; Ding, J.; Liu, W.; Ma, Y.; Zhu, W.; Meng, S.; Liang, C.; Cai, Q. Effect in situ phase reaction of η M12C and M6C on microstructure and mechanical properties of tungsten heavy alloy via spark plasma sintering. *Int. J. Refract. Met. Hard Mater.* **2023**, *114*, 106251. [CrossRef]
72. Frost, H.J.; Ashby, M.F. *Deformation-Mechanism Maps*; Pergamon Press: London, UK, 1982; 328p.
73. Young, W.S.; Culter, I.B. Initial sintering with constant rates of heating. *J. Am. Ceram. Soc.* **1970**, *53*, 659–663. [CrossRef]
74. Coble, R. A model for boundary diffusion controlled creep in polycrystalline materials. *J. Appl. Phys.* **1963**, *34*, 1679–1682. [CrossRef]
75. Lantsev, E.A.; Malekhonova, N.V.; Nokhrin, A.V.; Chuvil'deev, V.N.; Boldin, M.S.; Blagoveshchenskiy, Y.V.; Andreev, P.V.; Smetanina, K.E.; Isaeva, N.V.; Shotin, S.V. Influence of oxygen on densification kinetics of WC nanopowders during SPS. *Ceram. Int.* **2021**, *47*, 4294–4309. [CrossRef]
76. Lantsev, E.A.; Malekhonova, N.V.; Nokhrin, A.V.; Chuvil'deev, V.N.; Boldin, M.S.; Blagoveshchenskiy, Y.V.; Andreev, P.V.; Smetanina, K.E.; Isaeva, N.V.; Murashov, A.A. Spark plasma sintering of fine-grained WC hard alloys with ultra-low cobalt content. *J. Alloys Compd.* **2021**, *857*, 157535. [CrossRef]
77. Lantcev, E.; Nokhrin, A.; Malekhonova, N.; Boldin, M.; Chuvil'deev, V.; Blagoveshchenskiy, Y.; Isaeva, N.; Andreev, P.; Smetanina, K.; Murashov, A. A study of the impact of graphite on the kinetics of SPS in nano- and submicron WC-10%Co powder compositions. *Ceramics* **2021**, *4*, 331–363. [CrossRef]
78. Golovkina, L.S.; Orlova, A.I.; Nokhrin, A.V.; Boldin, M.S.; Lantsev, E.A.; Chuvil'deev, V.N.; Sakharov, N.V.; Shotin, S.V.; Zelenov, A.Y. Spark Plasma Sintering of fine-grained ceramic-metal composites YAG:Nd-(W,Mo) based on garnet-type oxide Y2.5Nd0.5Al5O12 for inert matrix fuel. *J. Nucl. Mater.* **2018**, *511*, 109–121. [CrossRef]
79. Kolobov, Y.R.; Grabovetskaya, G.P.; Ivanov, K.V.; Girsova, N.V. Effect of the grain-boundary state and grain size on the mechanisms of creep of submicrocrystalline nickel. *Phys. Met. Metallogr.* **2001**, *91*, 532–537. (In Russian)
80. Chuvil'deev, V.N.; Boldin, M.S.; Dyatlova, Y.G.; Rumyantsev, V.I.; Ordanyan, S.S. A comparative study of hot pressing and Spark Plasma Sintering of Al_2O_3-ZrO_2-Ti(C,N) powders. *Inorg. Mater.* **2015**, *51*, 1047–1053. [CrossRef]
81. Chuvil'deev, V.N.; Blagoveshchenskiy, Y.V.; Nokhrin, A.V.; Boldin, M.S.; Sakharov, N.V.; Isaeva, N.V.; Shotin, S.V.; Belkin, O.A.; Popov, A.A.; Smirnova, E.S.; et al. Spark plasma sintering of tungsten carbide nanopowders obtained through DC arc plasma synthesis. *J. Alloys Compd.* **2017**, *708*, 547–561. [CrossRef]
82. Golovkina, L.S.; Orlova, A.I.; Nokhrin, A.V.; Boldin, M.S.; Chuvil'deev, V.N.; Sakharov, N.V.; Belkin, O.A.; Shotin, S.V.; Zelenov, A.Y. Spark Plasma Sintering of fine-grain ceramic-metal composites based on garnet-structure oxide $Y_{2.5}Nd_{0.5}Al_5O_{12}$ for Inert Matrix Fuel. *Mater. Chem. Phys.* **2018**, *214*, 516–526. [CrossRef]
83. Segal, V.M.; Beyerlein, I.J.; Tome, C.N.; Chuvil'deev, V.N.; Kopylov, V.I. *Fundamentals and Engineering of Severe Plastic Deformation*; Nova Science Publishers: New York, NY, USA, 2010; 542p.
84. Blaine, D.C.; Park, S.J.; Suri, P.; German, R.M. Application of work-of-sintering concepts in powder metals. *Metall. Mater. Trans. A* **2006**, *37*, 2827–2835. [CrossRef]
85. Park, S.J.; Johnson, J.L.; Wu, Y.; Kwon, Y.-S.; Lee, S.; German, M.R. Analysis of the effect of solubility on the densification behavior of tungsten heavy alloys using the master sintering curve approach. *Int. J. Refract. Met. Hard Mater.* **2013**, *37*, 52–59. [CrossRef]
86. Hu, K.; Li, X.; Qu, S.; Li, Y. Effect of heating rate on densification and grain growth during spark plasma sintering of 93W-5.6Ni-1.4Fe heavy alloys. *Metall. Mater. Trans. A* **2013**, *44*, 4323–4336. [CrossRef]
87. Larikov, L.N.; Yurchenko, Y.F. *Diffusion in Metals and Alloys*; Naukova Dumka: Kiev, Ukraine, 1987; 509p. (In Russian)
88. Park, S.M.; Martin, J.M.; Guo, J.F.; Johnson, J.L. Densification behavior of tungsten heavy alloy based on master sintering curve concept. *Metall. Mater. Trans. A* **2006**, *37*, 2837–2848. [CrossRef]
89. Seith, W. *Diffusion in Mettallen. Platzwechselreaktionen*; Springer: Berlin/Heidelberg, Germany, 1955; 381p.

Disclaimer/Publisher's Note: The statements, opinions and data contained in all publications are solely those of the individual author(s) and contributor(s) and not of MDPI and/or the editor(s). MDPI and/or the editor(s) disclaim responsibility for any injury to people or property resulting from any ideas, methods, instructions or products referred to in the content.